Check for updates

JGR Earth Surface

RESEARCH ARTICLE
10.1029/2025JF008556

Well-Posed Debris-Flow Models With Phase Separation

X. Meng[1,2], L. Zhao[3], C. G. Johnson[4], and J. M. N. T. Gray[4]

[1]Centre for Ports and Maritime Safety, Dalian Maritime University, Dalian, PR China, [2]Department of Civil Engineering, Dalian Maritime University, Dalian, PR China, [3]Navigation College, Dalian Maritime University, Dalian, PR China, [4]Department of Mathematics and Manchester Centre for Nonlinear Dynamics, University of Manchester, Manchester, UK

Key Points:

- Depth-averaged viscous terms are included into the debris-flow model of Meng et al. (https://doi.org/10.1017/jfm.2022.400) to ensure that it is mathematically well-posed
- In the absence of viscous terms, it is shown that ill-posed regions develop and the numerical solutions do not converge on grid refinement
- Three model variants are used to illustrate the inclusion of relative species motion, vertical flow structure, and velocity shear

Supporting Information:

Supporting Information may be found in the online version of this article.

Correspondence to:

J. M. N. T. Gray,
nico.gray@manchester.ac.uk

Citation:

Meng, X., Zhao, L., Johnson, C. G., & Gray, J. M. N. T. (2026). Well-posed debris-flow models with phase separation. *Journal of Geophysical Research: Earth Surface*, *131*, e2025JF008556. https://doi.org/10.1029/2025JF008556

Received 13 MAY 2025
Accepted 23 SEP 2026

Author Contributions:

Conceptualization: X. Meng, J. M. N. T. Gray
Formal analysis: X. Meng, L. Zhao, J. M. N. T. Gray
Funding acquisition: X. Meng
Methodology: X. Meng
Software: L. Zhao
Supervision: C. G. Johnson, J. M. N. T. Gray
Validation: L. Zhao
Writing – original draft: X. Meng
Writing – review & editing: C. G. Johnson, J. M. N. T. Gray

© 2026 The Author(s). Journal of Geophysical Research: Earth Surface published by Wiley Periodicals LLC on behalf of American Geophysical Union. This is an open access article under the terms of the Creative Commons Attribution License, which permits use, distribution and reproduction in any medium, provided the original work is properly cited.

Abstract Debris flows pose a severe hazard to people and infrastructure in mountainous regions and are prone to phase separation. This can be captured by the depth-averaged multiphase theory of Meng et al. (https://doi.org/10.1017/jfm.2022.400), which accounts for vertical structure, velocity shear, and relative motion between the grains and fluid. To ensure well-posedness, depth-averaged viscous terms are included, and a high-resolution numerical scheme is formulated and implemented to solve the equations. Assuming the grains shear through their depth, the theory is able to capture the infiltration of fluid into the grains and subsequent evolution into a steadily traveling wave with a deep dry front and a progressively fluid-rich tail. Crucially, it is shown that in the absence of the diffusive terms, the model develops ill-posed regions, in which the numerical solution does not converge on grid refinement. In the absence of velocity shear, a deep dry front does not form, and the solution stretches out. A reduced composite model is derived and compared against two multiphase variants: (a) plug flow and (b) linear shear with basal slip in the grains. Quantitative comparisons are made to the experiments of Taylor-Noonan et al. (https://doi.org/10.1029/2022jf006622). The composite model advances more slowly than either multiphase variant, yet its deposit center of mass lies farthest downstream, while the longest runout occurs with the plug-flow multiphase model. The best overall agreement is with the multiphase model with linear shear and basal slip.

Plain Language Summary Field observations show that debris-flow fronts are often thicker and drier than their tails. This is an example of phase-separation, in which large grains and muddy fluid separate from one another during flow. In this paper, a mathematical model that can capture this behavior is investigated. It has the capability to resolve (a) the vertical structure of the flow (i.e., whether the fluid free-surface lies above or below the granular free-surface), (b) shear within the body of grains and/or fluid (i.e., whether the top of the flow is moving faster than the base), and (c) mobility differences between the fluid and grains (which can lead to one phase getting ahead of the other). It is shown that all three processes are important for generating a thick dry granular front, and a more fluid-rich tail, as the debris flow moves down slope. The paper also shows that it is necessary to include viscous terms in the grain and fluid momentum balances, otherwise a resonance between the equations can lead to catastrophic instabilities in certain areas of parameter space, which render numerical solutions invalid. This is overlooked in most debris-flow models.

1. Introduction

Debris flows are complex mixtures of rock, soil, wood, and water that flow rapidly down mountainous slopes, and pose a significant threat to people and infrastructure throughout the world. Their frequency has increased in recent years due to a greater number of high-rainfall-intensity events, linked to climate change, and the melting of glaciers and permafrost, which increases the amount of source material and destabilizes previously stable slopes. Typical examples include a catastrophic debris flow which occurred in the Chamoli district of Uttarakhand, India in February 2021, following the collapse of a glacier in the Nanda Devi region (Shugar et al., 2021). This event caused severe damage to two hydropower projects and resulted in the loss of at least 200 lives. Massive debris flows also occurred in Montecito, California, in 2018, and were triggered by heavy rainfall following the Thomas Fire (Lukashov et al., 2019). This resulted in the destruction of over 100 homes and the tragic loss of 23 lives. These incidents highlight the urgent need to develop and enhance debris flow models for hazard risk assessment.

Debris flows are often characterized by deep, dry, bouldery fronts followed by progressively thinner, more fluid-rich tails that have a finer-grained size distribution (Iverson, 1997; Pierson, 1986). Debris flows can also destabilize into a series of boulder-rich surges interspersed with muddy or fluid-rich flows (Kean et al., 2013). Accurate modeling of debris flow motion requires consideration of this phase separation, as it significantly

21699011, 2026, 10, Downloaded from https://agupubs.onlinelibrary.wiley.com/doi/10.1029/2025JF008556 by The University Of Manchester, Wiley Online Library on [18/10/2026]. See the Terms and Conditions (https://onlinelibrary.wiley.com/terms-and-conditions) on Wiley Online Library for rules of use; OA articles are governed by the applicable Creative Commons License

impacts flow mobility by altering spatial compositions. Iverson (2003) argued that debris flow models that used a single-phase constitutive model (e.g., between stress and strain-rate) were unable to accurately capture debris flow motion, because the flow composition, and/or particle-size distribution, significantly change the local rheological properties, that is, "a single debris-flow rheology was a myth." Instead, Iverson (2003) suggested that multiphase depth-averaged frameworks provided a more effective approach for capturing their heterogeneous nature.

Most existing debris flow models follow Savage and Hutter's (1989) depth-averaged approach for dry granular flows, in which the equations are derived by making a shallow-layer approximation (i.e., the characteristic flow depth is much smaller than the characteristic flow length). However, rather than consisting of a single pair of depth-averaged mass and momentum balances, multiphase debris-flow models typically have two, or more, pairs of depth-averaged mass and momentum balances, one set for each phase. In addition, the presence of the pore fluid, and/or the local grain-size distribution, introduces additional complexity by reducing/changing the basal granular friction and altering the flow mobility. Representative multiphase debris-flow models include: Iverson and Denlinger (2001), Pitman and Le (2005), Pelanti et al. (2008), Pudasaini (2012), Iverson and George (2014), Bouchut et al. (2016), Meng and Wang (2018), Pudasaini and Mergili (2019), and Meng et al. (2022). Iverson and George (2014) took account of the coupling between granular dilatancy and excess-pore-fluid pressure. Their model allows the species to separate in the vertical direction, but they move down slope together. Pitman and Le (2005) allowed grains and fluid to separate longitudinally by accounting for the velocity differences that arise from their distinct frictional properties (hereafter referred to as mobility-difference driven transport). Similar approaches were adopted in the models of Pelanti et al. (2008) and Pudasaini (2012), with the latter also incorporating the added mass effect. This accounts for the influence of acceleration differences between the solid and fluid phases. Further advances were made by Bouchut et al. (2016) and Sun and Wang (2024), who introduced granular dilatancy laws alongside mobility-difference transport. These models allow grains and fluid to separate in the vertical direction due to granular dilatancy, and in the downslope direction due to mobility differences.

Although these multiphase debris-flow models incorporate more physics and are necessary to accurately describe the evolving composition of the material, they are also plagued by resonances between the equations that lead to catastrophic short-wavelength instabilities. This is known as ill-posedness, and is a significant concern because most multiphase debris-flow models contain regions of parameter space where the equations are ill-posed (Langham et al., 2025a, 2025b). The resonances occur when the underlying characteristics of the Jacobian matrix associated with the flux function, that is, the eigenvalues that determine the propagation speeds of infinitesimal disturbances, coincide, or when these wave speeds become complex, which results in small amplitude perturbations growing at an unbounded rate in the high-wavenumber (short-wavelength) limit (Ovsyannikov, 1979; Joseph & Saut, 1990; Langham et al., 2025a, 2025b). Ill-posed regions of parameter space are disastrous for numerical methods, because within them results may look plausible at a given resolution, but on grid refinement they do not converge to a solution, as one would expect, but instead resolve finer and finer detail, that becomes progressively more unstable. Fundamentally, no solution exists in these ill-posed regions (Langham et al., 2025a, 2025b). Ill-posedness often occurs when developing new mathematical models, but it is rarely discussed and often overlooked. This is a mistake, because it is a clear indication that there is some important missing physics.

Inspiration can be taken from particle-size segregation in dry granular materials where well-posed multiphase models have been successfully developed. These models are also interesting because they have a more sophisticated treatment of differential particle transport due to vertical structure and velocity shear (Gray & Kokelaar, 2010). In this literature, it is now understood how particle-size segregation leads to the formation of bouldery fronts and finer grained tails, which is also directly relevant to debris flows (Edwards et al., 2023; Gray, 2018; Gray & Ancey, 2009; Gray & Kokelaar, 2010; Johnson et al., 2012). Essentially, large grains segregate to the flow surface, which moves faster than the base, so large grains are preferentially transported toward the flow front. Here they can be overrun, but re-segregate toward the surface and are recirculated and accumulated. Conversely, finer grains segregate to the slower moving base of the flow, are caught up by the advancing tail where they are also re-segregated and accumulated.

Since large-rich granular fronts are more frictional than the finer grained material behind, the flow front tends to bow upwards to create a deep surge front (Barker et al., 2021; Denissen et al., 2019). In two-dimensional depth-averaged simulations on an inclined plane, this frictional feedback can cause the flow to spontaneously break into

21699011, 2026, 10, Downloaded from https://agupubs.onlinelibrary.wiley.com/doi/10.1029/2025JF008556 by The University Of Manchester, Wiley Online Library on [18/10/2026]. See the Terms and Conditions (https://onlinelibrary.wiley.com/terms-and-conditions) on Wiley Online Library for rules of use; OA articles are governed by the applicable Creative Commons License

one or more fingers (Baker, Johnson, & Gray, 2016; Pouliquen et al., 1997; Woodhouse et al., 2012). The early fingering model of Woodhouse et al. (2012) dramatically illustrates the effect of ill-posedness (see their Figure 8), as the computed finger wavelength is entirely dependent on the numerical grid resolution. The remedy was to include additional details of the depth-averaged granular rheology, so that the viscous diffusion was set by a physical process, rather than by the grid-resolution-dependent diffusion inherent in the numerical method (Baker, Barker, & Gray, 2016; Gray & Edwards, 2014). This approach killed off the unbounded growth of the instability in the high-wavenumber limit, rendering the system well-posed, and allowing grid-resolved fingers to be computed (Baker, Johnson, & Gray, 2016).

As well as being well-posed, these depth-averaged granular segregation models introduce a mechanism for phase separation (i.e., via the combination of vertical-structure and velocity-shear), which is neglected in most debris-flow models. Motivated by this, Meng et al. (2022) developed a more general multiphase theory for phase separation in debris flows. The flow was assumed to be either undersaturated, or oversaturated, dependent on whether the grain free-surface lay above, or below, the fluid free-surface, and both the downslope grain and the fluid velocities had a profile through their depth. These assumptions allowed the vertical fluid-grain structure and the velocity-shear to be captured, as well as allowing differential motion due to mobility differences between the grains and the fluid. Meng et al.'s (2022) model successfully explained the steadily traveling waves observed in the experiments of Davies (1990), which have a dry granular front that smoothly transitions through the undersaturated, oversaturated, and pure fluid regimes as one moves to the rear of the flow.

Meng et al.'s (2022) model consisted of a pair of depth-averaged mass and momentum balances for both the granular and fluid phases. The equations switched from a conservative system into a non-conservative one as the flow transitioned from undersaturated to oversaturated regimes. Non-conservative terms are a potential problem, because it is not immediately clear how to formulate momentum jump conditions if discontinuities (shocks) develop (Chadwick, 1976). Meng et al. (2024) therefore introduced modifications to Meng et al.'s (2022) model, to ensure that the depth-averaged equations remain conservative within the oversaturated regime. This adjustment was particularly suitable for their focus on the experiments of Taylor-Noonan et al. (2022), where the flow is predominantly undersaturated, and the influence of the oversaturated region was minimal. Numerical results in Meng et al. (2024) quantitatively captured the transient experimental flows, which exhibited strong phase separation (Taylor-Noonan et al., 2022). The experiments were performed with monodisperse grains of diameter approximately equal to 3.85 mm, which facilitated the rapid dissipation of excess pore fluid pressures. The results therefore showed that dry fronts could form without the need to invoke excess-pore-fluid pressure feedback or particle-size segregation. These findings demonstrated that vertical structure of the flow, coupled with velocity shear, plays a pivotal role in the formation of dry granular fronts in debris flows.

While the model of Meng et al. (2024) was in conservative form and mathematically well-posed, it compromised the representation of the physics in the oversaturated regime. This paper therefore returns to the original formulation of Meng et al. (2022) and supplements it with a depth-averaged granular viscous term. The inclusion of viscous terms in both the granular and fluid momentum balances changes the mathematical character of the equations: The inviscid system is either of hyperbolic or of mixed type (dependent on whether the equations are well or ill-posed), while the viscous system implies that the resulting convection–diffusion equations are parabolic. This also implies that discontinuous shocks, which can develop in the inviscid hyperbolic system, are smoothed over a finite width, with sharp, but smooth, transitions being interpreted as diffuse shocks. The inclusion of viscosity therefore removes the ambiguity associated with imposing jump conditions across discontinuities in a non-conservative hyperbolic system and also guarantees that the equations are mathematically well-posed (Langham et al., 2025a, 2025b). In Section 4, it is shown that this well-posed model can be used to calculate the infiltration of a fluid into a static pile of grains, and the subsequent time-dependent development of a steadily propagating wave. Moreover, if there is velocity shear in the grains, a large amplitude dry front is formed that is followed by a fluid-rich tail as observed in Davies's (1990) experiments. On the other hand, if both the fluid and grains are assumed to have plug-like velocity profiles (i.e., no velocity shear) the flow stretches out and there is only a tiny dry front that does not bow upwards. Importantly, in Section 4.3, it is explicitly shown that these solutions are grid converged, whereas similar computations in the absence of viscous regularization produce grid-dependent results that are progressively more unstable and finer scaled as the grid is refined. This is typical of the behavior of an ill-posed model, and illustrates the type of behavior to be cautious of in debris-flow models that do not include viscous terms.

21699011, 2026, 10, Downloaded from https://agupubs.onlinelibrary.wiley.com/doi/10.1029/2025JF008556 by The University Of Manchester, Wiley Online Library on [18/10/2026]. See the Terms and Conditions (https://onlinelibrary.wiley.com/terms-and-conditions) on Wiley Online Library for rules of use; OA articles are governed by the applicable Creative Commons License

To illustrate the importance of (a) vertical structure, (b) velocity shear, and (c) mobility differences, three variants of Meng et al.'s (2022) extended model are used in Section 5 to model Taylor-Noonan et al.'s (2022) experiments. At the simplest level is a composite debris-flow model, that is derived in Section 2.2, and which assumes a fully saturated mixture in which the grains and fluid move together. The grains and fluid are therefore treated as a single composite material phase. This provides a basic benchmark to test the multiphase models against. The second variant is multiphase, resolves the vertical structure and assumes plug flow profiles for the grains and fluid. It is representative of many debris-flow models where the species move relative to one another due to mobility differences alone (see, e.g., Bouchut et al., 2016; Iverson & George, 2014; Meng & Wang, 2018; Pelanti et al., 2008; Pitman & Le, 2005; Pudasaini, 2012). The third variant additionally assumes that the grains can shear through their depth, which gives rise to a non-standard Darcy drag interaction term. It is this final version of the theory that has both mobility and shear driven species transport. The three model variants are therefore constructed to create a hierarchy of models with increasingly complex physics.

2. Governing Equations

2.1. Extended Well-Posed Theory of Meng et al. (2022)

A terrain-following orthogonal curvilinear coordinate system, $oxyz$, is defined with its origin located at the top of the inclined chute, as sketched in Figure 1. In this coordinate system, the x axis aligns with the downslope direction, the y axis lies along the cross-slope direction, and the z axis is the upward pointing normal to the chute (see, e.g., Savage & Hutter, 1991; Viroulet et al., 2017). It is assumed that there is no variation of the chute in the cross-slope direction, so the local inclination angle ζ is just a function of x. The base lies along $z = 0$ and the thicknesses of the grains h^g and fluid h^f are measured normal to the chute. This representation allows interpenetrating regions of grains and fluid to be defined, with regions of undersaturated and oversaturated grains, as well as regions of pure fluid and dry grains. Since air is implicitly assumed to occupy regions of dry grains, Meng et al.'s (2022) theory describes the motion of three phases.

In the undersaturated regime (when $h^g > h^f$), a dry surface layer of grains exists above the fluid-saturated granular layer beneath. The granular and fluid volume fractions are

$$\phi^g = \phi^c, \quad 0 \le z < h^g, \qquad \phi^f = \begin{cases} 0, & h^f \le z < h^g, \\ 1 - \phi^c, & 0 \le z < h^f, \end{cases} \tag{1a, b}$$

respectively, where the solids volume fraction ϕ^c is assumed to be constant. In the oversaturated regime (when $h^g \le h^f$), there is a pure fluid layer above a fluid saturated granular layer, that also has solids volume fraction ϕ^c, that is

$$\phi^g = \phi^c, \quad 0 \le z < h^g, \qquad \phi^f = \begin{cases} 1, & h^g \le z < h^f, \\ 1 - \phi^c, & 0 \le z < h^g. \end{cases} \tag{2a, b}$$

It follows from Equations 1a and 2a that the depth-averaged solids volume fraction (through the depth of the grains)

$$\bar{\phi}^g = \frac{1}{h^g} \int_0^{h^g} \phi^g \, dz = \phi^c, \tag{3}$$

which is constant across both the undersaturated and oversaturated regimes. However, the depth-averaged fluid volume fraction (through the depth of the fluid) depends on whether the flow is under- or over-saturated

$$\bar{\phi}^f = \frac{1}{h^f} \int_0^{h^f} \phi^f \, dz = \begin{cases} 1 - \phi^c, & h^f < h^g, \\ 1 - \phi^c h^g / h^f, & h^g \le h^f. \end{cases} \tag{4}$$

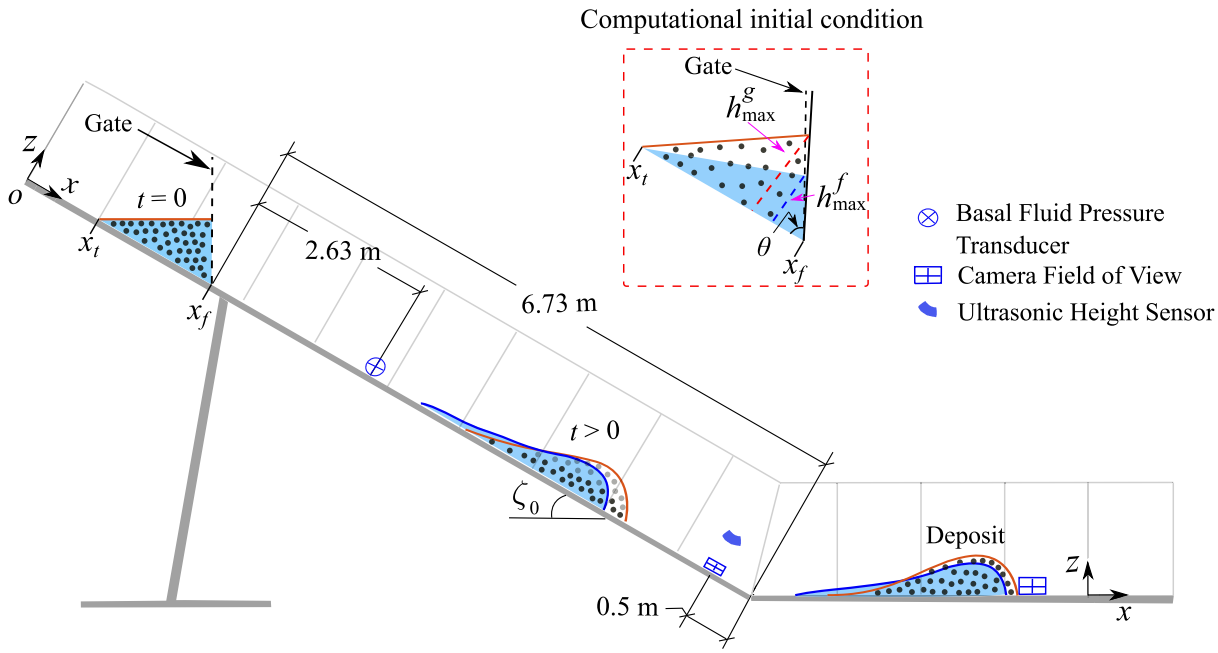


Figure 1. A schematic diagram illustrating the terrain-following curvilinear coordinate system *oxz* used in this paper. The *x* axis points locally down slope, and lies at an angle ζ to the horizontal, while the *z* axis is aligned with the upward pointing slope normal. At the various stages of motion, the granular and fluid free-surfaces are shown by red and blue lines, respectively. In addition, the region occupied by the fluid is shaded blue, and the granular region is denoted with circular markers that are shaded light gray, if they are being sheared forwards toward the front, and dark gray if they are stationary or are moving backwards relative to the front. Specific measurements are included for the modeling of the flume experiments of Taylor-Noonan et al. (2022) on a $\zeta_0 = 30°$ chute. The inset diagram shows the initial configuration used for computations. The diagram is reproduced with some modifications from Meng et al. (2024).

To unify these two regimes, the ratio of the internal interface height $s = \min(h^g, h^f)$ to the fluid height is defined as

$$\mathcal{H} = \frac{\min(h^f, h^g)}{h^f}. \tag{5}$$

The depth-averaged fluid volume fraction can then be expressed as

$$\bar{\phi}^f = 1 - \phi^c \mathcal{H}, \tag{6}$$

which has the advantage that it enables a unified framework to be constructed for describing both the undersaturated and the oversaturated flows. This contrasts with earlier theories, such as those of Meng et al. (2017), Bouchut et al. (2016), and Sun et al. (2023), which are restricted to either undersaturated or oversaturated regimes.

The grains and fluid are assumed to be incompressible with constant intrinsic densities $\varrho^{g\star}$ and $\varrho^{f\star}$, respectively, so that the density ratio $\gamma = \varrho^{f\star}/\varrho^{g\star}$. Meng et al. (2022) defined the volume-fraction-weighted depth-averaged granular and fluid velocities by

$$\bar{u}^g = \frac{\frac{1}{h^g}\int_0^{h^g} \phi^g u^g \, dz}{\frac{1}{h^g}\int_0^{h^g} \phi^g \, dz} = \frac{\overline{\phi^g u^g}}{\overline{\phi^g}}, \qquad \bar{u}^f = \frac{\frac{1}{h^f}\int_0^{h^f} \phi^f u^f \, dz}{\frac{1}{h^f}\int_0^{h^f} \phi^f \, dz} = \frac{\overline{\phi^f u^f}}{\overline{\phi^f}}, \tag{7a, b}$$

which allow the unified depth-averaged granular and fluid mass and momentum balances to be expressed as

$$\frac{\partial}{\partial t}(h^g \phi^c) + \frac{\partial}{\partial x}(h^g \phi^c \bar{u}^g) = 0, \tag{8}$$

21699011, 2026, 10, Downloaded from https://agupubs.onlinelibrary.wiley.com/doi/10.1029/2025JF008556 by The University Of Manchester, Wiley Online Library on [18/10/2026]. See the Terms and Conditions (https://onlinelibrary.wiley.com/terms-and-conditions) on Wiley Online Library for rules of use; OA articles are governed by the applicable Creative Commons License

$$\frac{\partial}{\partial t}\left(h^g\phi^c\bar{u}^g\right)+\frac{\partial}{\partial x}\left(\chi^g h^g\phi^c\left(\bar{u}^g\right)^2+\frac{1}{2}\left(h^g\right)^2\phi^c g\cos\zeta-\frac{1}{2}\gamma\phi^c\left(h^f\mathcal{H}\right)^2 g\cos\zeta\right)=S^g, \tag{9}$$

$$\frac{\partial}{\partial t}\left(h^f\bar{\phi}^f\right)+\frac{\partial}{\partial x}\left(h^f\bar{\phi}^f\bar{u}^f\right)=0, \tag{10}$$

$$\frac{\partial}{\partial t}\left(h^f\bar{\phi}^f\bar{u}^f\right)+\frac{\partial}{\partial x}\left(\chi^f h^f\bar{\phi}^f\left(\bar{u}^f\right)^2+\frac{1}{2}\left(h^f\right)^2 g\cos\zeta\right)=S^f, \tag{11}$$

where g is the constant of gravity acceleration, and the granular and fluid shape factors

$$\chi^g=\frac{\overline{\left(u^g\right)^2}}{\left(\bar{u}^g\right)^2},\qquad \chi^f=\frac{\overline{\phi^f\left(u^f\right)^2}}{\bar{\phi}^f\left(\bar{u}^f\right)^2}, \tag{12}$$

characterize the ratio of the depth-averaged velocity squared to the square of the depth-averaged velocity. For sheared velocity profiles the shape factors are non-unity, but this precludes the formation of grain or fluid free regions. Saingier et al. (2016) argued that this was unphysical, and so $\chi^\nu\approx 1$ near a front, but could be non-unity in thicker parts of the flow. They also showed that this only makes a difference to the front shape at high Froude numbers when inertia effects become significant. This paper therefore assumes that $\chi^g=\chi^f=1$, which is consistent with virtually all debris-flow models.

On the right-hand side of the momentum balance Equations 9 and 11 the generalized source terms, S^g and S^f, collect together the standard source terms, $\mathcal{L}^g$ and $\mathcal{L}^f$ (defined shortly), with the remaining non-conservative and diffusive terms

$$S^g=\mathcal{L}^g-\underbrace{\gamma\phi^c\mathcal{H}h^f g\cos\zeta\frac{\partial h^f}{\partial x}}_{\text{Buoyancy}}+\underbrace{\frac{\partial}{\partial x}\left(2\nu^g h^g\phi^c\frac{\partial\bar{u}^g}{\partial x}\right)}_{\text{Granular viscous term}}, \tag{13}$$

$$S^f=\mathcal{L}^f+\underbrace{\phi^c\mathcal{H}h^f g\cos\zeta\frac{\partial h^f}{\partial x}}_{\text{Buoyancy}}+\underbrace{\frac{\partial}{\partial x}\left(2\nu^f h^f\bar{\phi}^f\frac{\partial\bar{u}^f}{\partial x}\right)}_{\text{Fluid viscous term}}, \tag{14}$$

where ν^f is the constant kinematic viscosity of the fluid and the depth-averaged granular kinematic viscosity

$$\nu^g=\frac{1}{2}\hat{\nu}^g\left(h^g\right)^{\frac{1}{2}} \tag{15}$$

is derived from the $\mu(I)$-rheology for granular flows (GDR-MiDi, 2004; Gray & Edwards, 2014; Jop et al., 2006). The coefficient $\hat{\nu}^g$ naturally emerges from this derivation and is slope angle dependent, and defined only in the range of angles where dry steady-uniform flows develop. The addition of the fluid phase dramatically changes the range of angles over which the grains can flow, so the precise form of $\hat{\nu}^g$ remains unclear and warrants further investigation. For the purposes of this paper $\hat{\nu}^g$ is assumed to be a constant and the same value is used on both the inclined and horizontal sections. The primary role of including the granular viscosity is to ensure that the system as a whole has a diagonal diffusion operator, with strictly positive diffusion coefficients in each momentum equation. This structure renders the theory unconditionally well-posed (Langham et al., 2025a, 2025b), and has the added benefit of changing the mathematical character of the equations from a hyperbolic/mixed system to a parabolic convection–diffusion system, in which steep gradients are smoothed over a finite width. Developing and calibrating a physically complete slope-dependent granular viscosity is left for future work.

The standard source terms in Equations 13 and 14 are given by

21699011, 2026, 10, Downloaded from https://agupubs.onlinelibrary.wiley.com/doi/10.1029/2025JF008556 by The University Of Manchester, Wiley Online Library on [18/10/2026]. See the Terms and Conditions (https://onlinelibrary.wiley.com/terms-and-conditions) on Wiley Online Library for rules of use; OA articles are governed by the applicable Creative Commons License

$$\mathcal{L}^g = \underbrace{h^g \phi^c g \sin\zeta}_{\text{Gravity}} - \underbrace{\frac{\bar{u}^g}{|\bar{u}^g|}\left(1 - \gamma\mathcal{H}\frac{h^f}{h^g}\right)\mu^b h^g \phi^c \left(g\cos\zeta + \kappa(\bar{u}^g)^2\right)}_{\text{Basal friction}} + \underbrace{\frac{C^d}{\varrho^{g\star}}\left(\psi^f(s) - \psi^g(s)\right)}_{\text{Darcy drag}}, \tag{16}$$

$$\mathcal{L}^f = \underbrace{h^f(1-\phi^c\mathcal{H})g\sin\zeta}_{\text{Gravity}} - \underbrace{C^f \bar{u}^f|\bar{u}^f|}_{\text{Friction}} - \underbrace{\frac{C^d}{\varrho^{f\star}}\left(\psi^f(s) - \psi^g(s)\right)}_{\text{Darcy drag}}, \tag{17}$$

where $\kappa = -\partial\zeta/\partial x$ is the curvature and the coefficients μ^b, C^d and C^f will be defined in Section 2.3. In the Darcy drag, s is the internal interface height between the lower layer of saturated-grains and either the dry-grains or pure fluid above. It is defined as

$$s = \mathcal{H}h^f = \begin{cases} h^f, & h^g > h^f, \quad \text{undersaturated}, \\ h^g, & h^g \le h^f, \quad \text{oversaturated}, \end{cases} \tag{18}$$

and the granular and fluid streamfunctions are

$$\psi^g(s) = \int_0^s u^g\, dz, \qquad \psi^f(s) = \int_0^s u^f\, dz, \tag{19}$$

respectively. This formulation of the Darcy drag is a central component of Meng et al.'s (2022) theory. In contrast to conventional debris-flow models, which typically assume plug flow through the depth (Bouchut et al., 2016; Iverson & Denlinger, 2001; Iverson & George, 2014; Meng & Wang, 2016; Pelanti et al., 2008; Pitman & Le, 2005; Pudasaini, 2012), the present approach evaluates the interphase momentum exchange through streamfunctions associated with the vertical velocity profiles. Based on the experiments of Davies (1990) and Taylor-Noonan et al. (2022), the downslope velocity profile through the flow depth for the granular and fluid phases is modeled using the power-law function

$$u^\nu(z) = \lambda^\nu \bar{u}^\nu\left(\alpha^\nu + (1-\alpha^\nu)\,\frac{1+2m^\nu}{1+m^\nu}\left[1 - \left(1 - \frac{z}{h^\nu}\right)^{\frac{1+m^\nu}{m^\nu}}\right]\right), \tag{20}$$

where the superscript constituent label ν, can either equal g for grains or f for fluid, just in the same way superscripts g and f are used to indicate the granular and fluid thicknesses and velocities. The factor λ^g is unity irrespective of whether the flow is undersaturated or oversaturated. The factor λ^f is taken in the form

$$\lambda^f = \frac{1-\phi^c\mathcal{H}}{1-\phi^c\mathcal{H} + \phi^c(1-\alpha^f)(1-\mathcal{H})\frac{m^f}{1+m^f}\left[1-(1-\mathcal{H})^{1+\frac{1}{m^f}}\right]}. \tag{21}$$

In the undersaturated regime, $\mathcal{H} = 1$ and thus λ^f reduces to unity. By contrast, in the oversaturated regime, λ^f takes a more intricate form, reflecting the role of $\mathcal{H}$ as the ratio of flow thicknesses. The corresponding streamfunction is

$$\psi^\nu(s) = \lambda^\nu \bar{u}^\nu h^\nu\left[\alpha^\nu\frac{s}{h^\nu} + \frac{1-\alpha^\nu}{1+m^\nu}\left((1+2m^\nu)\,\frac{s}{h^\nu} + m^\nu\left(1-\frac{s}{h^\nu}\right)^{2+\frac{1}{m^\nu}} - m^\nu\right)\right]. \tag{22}$$

This extends the downslope velocity profile and associated streamfunction proposed by Meng et al. (2024) to incorporate basal slip. The non-dimensional basal slip velocity is denoted by α^ν, while the parameter m^ν governs the shape of the velocity profile. For $m^\nu = 1$, the velocity profile is parabolic, which naturally emerges from the $\mu(J)$-rheology that characterizes granular suspension flows (Boyer et al., 2011; Guazzelli & Pouliquen, 2018). For $m^\nu = 2$, Equation 20 reduces to the classical Bagnold velocity profile for granular flows (GDR-MiDi, 2004; Gray

21699011, 2026, 10, Downloaded from https://agupubs.onlinelibrary.wiley.com/doi/10.1029/2025JF008556 by The University Of Manchester, Wiley Online Library on [18/10/2026]. See the Terms and Conditions (https://onlinelibrary.wiley.com/terms-and-conditions) on Wiley Online Library for rules of use; OA articles are governed by the applicable Creative Commons License

21699011, 2026, 10, Downloaded from https://agupubs.onlinelibrary.wiley.com/doi/10.1029/2025JF008556 by The University Of Manchester, Wiley Online Library on [18/10/2026]. See the Terms and Conditions (https://onlinelibrary.wiley.com/terms-and-conditions) on Wiley Online Library for rules of use; OA articles are governed by the applicable Creative Commons License

& Edwards, 2014; Jop et al., 2006), and as $m^{\nu} \to \infty$, the profile reduces to linear shear with basal slip, which has been extensively used to model shear-induced large particle transport in bidisperse granular materials (Baker, Johnson, & Gray, 2016; Gray & Kokelaar, 2010; Woodhouse et al., 2012). Finally, assuming $\alpha^{\nu} = 1$ implies that the velocity profile (Equation 20) is a plug, so if both the grains and the fluid have plug profiles, then the streamfunction difference reduces to a term proportional to the depth-averaged velocity difference, and the theory recovers the classical structure of two-phase debris-flow formulations (Bouchut et al., 2016; Iverson & George, 2014; Meng & Wang, 2016; Pelanti et al., 2008; Pitman & Le, 2005; Pudasaini, 2012). Meng et al.'s (2022) model therefore provides a versatile framework in which to study the effect of the assumed velocity profiles (Equation 20) through the flow depth.

2.2. Reduced Composite Debris-Flow Model

As well as being able to reduce Meng et al.'s (2022) model to standard two-phase formulations, it is useful to introduce a simplified composite model with a single velocity field for comparison. In this framework, debris flows are assumed to be a homogeneous mixture with constant species volume fractions, and no phase separation. The resulting model can be derived from the Meng et al.'s (2022) model by assuming that the Darcy drag coefficient, $C^{d} \to \infty$, so that

$$\bar{u}^{g} = \bar{u}^{f} = \bar{u} \tag{23}$$

and assuming that the grain and fluid heights coincide at a common thickness h (i.e., the flow is implicitly assumed to be fully saturated)

$$h^{g} = h^{f} = h, \qquad \Rightarrow \mathcal{H} \equiv 1. \tag{24}$$

Summing the depth-averaged granular and fluid mass balances (Equations 8 and 10) then implies the composite depth-averaged mass balance is

$$\frac{\partial h}{\partial t} + \frac{\partial}{\partial x}(h\bar{u}) = 0. \tag{25}$$

Similarly, multiplying the granular depth-averaged momentum balance (Equation 9) by $\varrho^{g\star}$ and the depth-averaged fluid momentum balance (Equation 11) by $\varrho^{f\star}$ and then dividing their sum by the bulk density

$$\varrho = \varrho^{g\star}\phi^{c} + \varrho^{f\star}(1-\phi^{c}), \tag{26}$$

gives the composite depth-averaged momentum balance

$$\frac{\partial}{\partial t}(h\bar{u}) + \frac{\partial}{\partial x}\left(\chi h\bar{u}^{2} + \frac{1}{2}h^{2}g\cos\zeta\right) = S + \underbrace{\frac{\partial}{\partial x}\left(2\nu h\frac{\partial \bar{u}}{\partial x}\right)}_{\text{Viscous term}}, \tag{27}$$

where χ is the shape factor (assumed equal to unity), the source term

$$S = \underbrace{hg\sin\zeta}_{\text{Gravity}} - \underbrace{\frac{\bar{u}}{|\bar{u}|}\left(\frac{\varrho^{g\star}-\varrho^{f\star}}{\varrho}\right)\mu^{b}h\phi^{c}\left(g\cos\zeta + \kappa\bar{u}^{2}\right)}_{\text{Granular basal friction}} - \underbrace{\frac{\varrho^{f\star}}{\varrho}C^{f}\bar{u}|\bar{u}|}_{\text{Fluid friction}}, \tag{28}$$

and the kinematic viscosity

$$\nu = \left(\frac{\varrho^{g\star}}{\varrho}\right)\phi^{c}\nu^{g} + \left(\frac{\varrho^{f\star}}{\varrho}\right)(1-\phi^{c})\nu^{f}, \tag{29}$$

21699011, 2026, 10, Downloaded from https://agupubs.onlinelibrary.wiley.com/doi/10.1029/2025JF008556 by The University Of Manchester, Wiley Online Library on [18/10/2026]. See the Terms and Conditions (https://onlinelibrary.wiley.com/terms-and-conditions) on Wiley Online Library for rules of use; OA articles are governed by the applicable Creative Commons License

where ν^g is defined in Equation 15. This theory could be thought of as a modified Savage and Hutter (1991) model in which the granular friction is reduced by the buoyancy induced by the presence of the interstitial fluid, or alternatively a simplified Iverson and Denlinger (2001) type system in which there are no excess pore pressure effects, and the viscosity now arises from both the grains and the fluid.

2.3. Basal Granular Friction, Basal Fluid Friction, and Darcy Drag

In this study, the basal granular friction coefficient μ^b, the basal fluid friction coefficient C^f, and the Darcy interaction drag coefficient C^d require further specification. On rough beds the basal friction is given by the dynamic friction law proposed by Pouliquen and Forterre (2002)

$$\mu^b = \mu_1 + \frac{\mu_2 - \mu_1}{1 + \frac{\beta h^g}{\mathcal{L} Fr}}, \tag{30}$$

where the Froude number is defined as

$$Fr = \frac{\bar{u}^g}{\sqrt{g h^g \cos\zeta}}, \tag{31}$$

and μ_1 and μ_2 represent the minimum and maximum effective basal friction coefficients, respectively, following Pouliquen and Forterre (2002). The parameter β is a dimensionless empirical constant controlling the transition between frictional regimes, and $\mathcal{L}$ is a characteristic length scale related to grain properties and flow thickness in the original calibration experiments. These parameters are discussed further in Section 4.1.

For open-channel water flows, the fluid basal friction coefficient, C^f, is typically related to the Manning equation (Manning, 1891) and is expressed as

$$C^f = \bar{\phi}^f \frac{g h^f n^2}{(R)^{4/3}}, \tag{32}$$

where n is the Manning coefficient and the factor $\bar{\phi}^f$ accounts for the partial occupancy of the pore fluid within the granular medium, ensuring that (Equation 32) reduces to the classical Manning equation for open-channel water flows in the absence of grains. The hydraulic radius R in Equation 32 is given by

$$R = \frac{W h^f}{W + 2h^f}. \tag{33}$$

For channels where the width is much greater than the typical flow depth, that is, $h^f \ll W$, the hydraulic radius simplifies to $R = h^f$. The basal drag coefficient then reduces to the Chézy formula with Manning coefficient

$$C^f = \bar{\phi}^f \frac{g n^2}{\left(h^f\right)^{1/3}}. \tag{34}$$

The Darcy drag describes the momentum exchange between grains and the pore fluid, and controls the permeability of the grain skeleton. In this paper, the Darcy drag coefficient is expressed as

$$C^d = \mu^f \frac{(1 - \phi^c)^2}{k}, \tag{35}$$

as applied by Iverson (1997) and Goharzadeh et al. (2005), where the fluid dynamic viscosity $\mu^f = \varrho^{f\star} \nu^f$ and the permeability $k = (1 - \phi^c)^3 d^2 / \left(180(\phi^c)^2\right)$ is determined by Carman's formula for the packing of spheres with diameter d (Carman, 1937).

3. Numerical Method

Meng et al.'s (2022) depth-averaged Equations 8–11 are solved numerically with the shock-capturing, non-oscillatory central scheme proposed by Kurganov and Tadmor (2000) in combination with the technique of Kurganov and Petrova (2009) to handle non-conservative product terms. The two-phase system is expressed in a standard form as

$$\frac{\partial \boldsymbol{U}}{\partial t}+\frac{\partial \boldsymbol{F}(\boldsymbol{U})}{\partial x}=\boldsymbol{S}(\boldsymbol{U})+\boldsymbol{N}(\boldsymbol{U},\boldsymbol{U}_x)+\frac{\partial \boldsymbol{D}(\boldsymbol{U},\boldsymbol{U}_x)}{\partial x}, \tag{36}$$

where $\boldsymbol{U}$ denotes the vector of conservative variables, $\boldsymbol{F}$ represents the convective flux vector, $\boldsymbol{S}$ denotes the source term vector, $\boldsymbol{N}$ characterizes the non-conservative terms, and $\boldsymbol{D}$ denotes the diffusive flux vector. The conservative variables $\boldsymbol{U}$ are defined as

$$\boldsymbol{U}=\left(H^g, M^g, H^f, M^f\right)^{\mathrm{T}}=\left(h^g\phi^c, h^g\phi^c\bar{u}^g, h^f\bar{\phi}^f, h^f\bar{\phi}^f\bar{u}^f\right)^{\mathrm{T}}. \tag{37}$$

Using the conservative variables defined in Equation 37, the convective flux vector $\boldsymbol{F}$, the source term vector $\boldsymbol{S}$, the non-conservative term vector $\boldsymbol{N}$ and the diffusive flux vector $\boldsymbol{D}$ are derived. Their detailed expressions are provided in Appendix A. Following Kurganov and Petrova (2009), the semi-discrete central scheme for the current system with non-conservative terms is formulated as

$$\frac{d}{dt}\overline{\boldsymbol{U}}_j(t)=-\frac{\boldsymbol{H}_{j+\frac{1}{2}}(t)-\boldsymbol{H}_{j-\frac{1}{2}}(t)}{\Delta x}+\overline{\boldsymbol{S}}_j(t)+\overline{\boldsymbol{N}}_j(t)+\frac{\boldsymbol{P}_{j+\frac{1}{2}}(t)-\boldsymbol{P}_{j-\frac{1}{2}}(t)}{\Delta x}, \tag{38}$$

where the cell averages of the source, the non-conservative terms and the viscous terms on the right-hand side are given by

$$\overline{\boldsymbol{S}}_j(t)=\frac{1}{\Delta x}\int_{x_{j-\frac{1}{2}}}^{x_{j+\frac{1}{2}}}\boldsymbol{S}dx, \qquad \overline{\boldsymbol{N}}_j(t)=\frac{1}{\Delta x}\int_{x_{j-\frac{1}{2}}}^{x_{j+\frac{1}{2}}}\boldsymbol{N}dx, \tag{39}$$

$$\boldsymbol{P}_{j+\frac{1}{2}}(t)=\frac{1}{2}\left[\boldsymbol{D}\left(\boldsymbol{U}_j(t),\frac{\boldsymbol{U}_{j+1}(t)-\boldsymbol{U}_j(t)}{\Delta x}\right)+\boldsymbol{D}\left(\boldsymbol{U}_{j+1}(t),\frac{\boldsymbol{U}_{j+1}(t)-\boldsymbol{U}_j(t)}{\Delta x}\right)\right], \tag{40}$$

for the cell $[x_{j-\frac{1}{2}}, x_{j+\frac{1}{2}}]$, respectively. The numerical fluxes are computed using a generalized minmod limiter with parameter $\theta = 1$ (Kurganov & Tadmor, 2000). This choice yields second-order accuracy in smooth regions and reduces to first order near discontinuities. The midpoint rule is used to estimate the integral of the source terms over the cell.

In the numerical simulations, physically dry or nearly dry granular or fluid regions are treated by imposing a small positive numerical floor $h^{\nu}_{\min} = 10^{-6}$ m on each phase. It ensures that the discrete phase thickness remains bounded below by $h^{\nu}_{\min}$ for $\nu = g, f$ and prevents division by vanishing thickness in the velocity computation. To preserve positivity of the reconstructed states, the correction procedure proposed by Chertock et al. (2015) is used. Whenever a reconstructed interface value becomes negative, the slope in that cell is flattened, and the interface values are reset to the corresponding cell average, that is,

$$(h^{\nu})^{-}_{j+\frac{1}{2}}=\bar{h}^{\nu}_j, \quad (h^{\nu})^{+}_{j-\frac{1}{2}}=\bar{h}^{\nu}_j, \quad \text{if} \quad (h^{\nu})^{-}_{j+\frac{1}{2}}<0 \quad \text{or} \quad (h^{\nu})^{+}_{j-\frac{1}{2}}<0. \tag{41}$$

For cells in which h^{ν} is close to $h^{\nu}_{\min}$, the fluid basal friction term $C^f\bar{u}^f|\bar{u}^f|$ may introduce numerical stiffness. To alleviate this difficulty, the fluid velocity appearing in the basal friction term is evaluated using the desingularization formula

$$\bar{u}^{\nu}_j=\frac{2H^{\nu}_j M^{\nu}_j}{\left(H^{\nu}_j\right)^2+\max\left(\left(H^{\nu}_j\right)^2,\varepsilon^2\right)}, \tag{42}$$

21699011, 2026, 10, Downloaded from https://agupubs.onlinelibrary.wiley.com/doi/10.1029/2025JF008556 by The University Of Manchester, Wiley Online Library on [18/10/2026]. See the Terms and Conditions (https://onlinelibrary.wiley.com/terms-and-conditions) on Wiley Online Library for rules of use; OA articles are governed by the applicable Creative Commons License

21699011, 2026, 10, Downloaded from https://agupubs.onlinelibrary.wiley.com/doi/10.1029/2025JF008556 by The University Of Manchester, Wiley Online Library on [18/10/2026]. See the Terms and Conditions (https://onlinelibrary.wiley.com/terms-and-conditions) on Wiley Online Library for rules of use; OA articles are governed by the applicable Creative Commons License

as proposed by Chertock et al. (2015) and used by Meng et al. (2024). The desingularization parameter $\varepsilon = 5 \times 10^{-5}$ m is selected such that its influence on the velocity reconstruction remains negligible when the flow thickness is non-trivially small. Alternatively, one could refer to adaptive mesh refinement techniques near the flow front to address the difficulty of computing velocities at small thickness, see Berger and LeVeque (1998) and Patra et al. (2005).

Developing a robust discretization method for non-conservative product terms in hyperbolic systems is notoriously challenging. In many cases, different discretization approaches for these terms can lead to qualitatively different computed solutions (Cauret et al., 1989), especially when shocks develop. In the present system, the grain and fluid viscous terms are included as part of the governing equations. They provide a regularizing mechanism that guarantees the well-posedness of the initial-boundary-value problem, which could otherwise become ill-posed in regions of solution space. In addition, jump discontinuities in the inviscid system are replaced by finite-width smooth transition layers (diffuse shocks). This inherent smoothness significantly reduces the sensitivity of the computed solution to the specific discretization of the non-conservative terms, thereby alleviating the computational challenges typically associated with their presence. In this study, the approach outlined in Kurganov and Petrova (2009) is adopted to discretize the non-conservative terms as follows:

$$\overline{\boldsymbol{N}}_j^{(2)} = \begin{cases} -\dfrac{\gamma\phi^c}{(1-\phi^c)^2} H_j^f g\cos\zeta \left(\dfrac{\partial H^f}{\partial x}\right)_j, & \text{(undersaturated)} \\ -\gamma H_j^g g\cos\zeta \left(\dfrac{\partial H^f}{\partial x} + \dfrac{\partial H^g}{\partial x}\right)_j, & \text{(oversaturated)} \end{cases} \tag{43}$$

and

$$\overline{\boldsymbol{N}}_j^{(4)} = -\overline{\boldsymbol{N}}_j^{(2)}/\gamma, \tag{44}$$

where the numerical derivatives $\left(\left(H^f\right)_x\right)_j$ and $\left(\left(H^g\right)_x\right)_j$ are computed using a minmod-like limiter to ensure the desired non-oscillatory property.

The temporal derivative on the left-hand side of the semi-discrete scheme (Equation 38) is advanced in time using the standard explicit third-order Runge–Kutta method. The time step is determined according to a Courant–Friedrichs–Lewy (CFL) condition with a CFL number of 0.1. Due to the presence of the diffusion term, an additional stability restriction is imposed. Accordingly, the time step is given by

$$\Delta t = \min\left(\frac{\Delta x}{|a|}CFL,\ \frac{(\Delta x)^2}{\max(\nu^f, \nu^g)}\right), \quad \text{where} \quad a = \max\{|\lambda_i|\}, \quad i = 1\ldots 4. \tag{45}$$

In addition, a conservative upper bound of $\Delta t \leq 10^{-6}$ s is imposed to ensure that the explicit third-order Runge–Kutta scheme operates well within its linear stability region. The characteristic wave speeds λ_i $(i = 1, \ldots, 4)$ are defined in Equations B2 and B5 for undersaturated and oversaturated flows, respectively. It should be noted that the influence of the non-conservative term on the characteristic wave speed is not considered in this analysis.

4. Time-Dependent Simulation of a Traveling Debris-Flow Wave

Davies's (1990) moving-bed flume experiments showed that it was possible to develop steadily traveling waves that have a deep dry resistive front that is pushed downslope by a thinner more fluid-rich tail. Meng et al. (2022) were able to quantitatively capture the wave shape, wave velocity, and the internal particle recirculation, using the steady-state multiphase depth-averaged theory with a shear profile through the grains (see Section 5 of Meng et al. (2022) for a full description of Davies's (1990) experiments as well as Sections 6.2 and 6.3 where a full comparison is made to the steadily-traveling wave solution). This section investigates the time-dependent evolution toward such steadily-traveling-wave states, and the effect of the assumed velocity profile on the solution. This is a challenging problem, because the solution simultaneously encompasses the dry, undersaturated,

21699011, 2026, 10, Downloaded from https://agupubs.onlinelibrary.wiley.com/doi/10.1029/2025JF008556 by The University Of Manchester, Wiley Online Library on [18/10/2026]. See the Terms and Conditions (https://onlinelibrary.wiley.com/terms-and-conditions) on Wiley Online Library for rules of use; OA articles are governed by the applicable Creative Commons License

oversaturated, and pure fluid regimes, and exhibits clear signs of ill-posedness if the depth-averaged viscous terms are not included in the model, as shall now be shown.

4.1. Set-Up and Parameters

Numerical simulations are conducted on a 20 m long chute that is inclined at an angle $\zeta = 15°$, which allows the dry grains to remain stationary. The origin of the terrain-following coordinate system oxz is defined at the upper inlet of the chute. At the inlet a steady uniform fluid inflow is prescribed of thickness $h^f(0,t) = h_0 = 0.00969241$ m. The inflow velocity is determined based on a steady uniform flow condition, expressed as $\bar{u}^f(0,t) = h_0^{\frac{2}{3}}\sqrt{\sin\zeta}/n$. Using the Manning coefficient $n = 0.0593$ s $\mathrm{m}^{-(1/3)}$ from Meng et al. (2022), the inflow velocity is calculated to be $\bar{u}^f(0,t) = u_0 = 0.39$ m/s. The computational parameters adopted in this study are as follows: gravitational acceleration $g = 9.8$ m/s^2; grain density $\varrho^{g\star} = 1{,}400$ kg/m^3; granular viscosity coefficient $\hat{\nu}^g = 1.79 \times 10^{-4}$ $\mathrm{m}^{\frac{3}{2}}$ s^{-1}; fluid density $\varrho^{f\star} = 1{,}000$ kg/m^3 (hence $\gamma = 0.714$); fluid dynamic viscosity $\mu^f = 0.0013$ Pa s; fluid kinematic viscosity $\nu^f = 1 \times 10^{-5}$ m^2 s^{-1}; basal friction coefficients $\mu_1 = \tan(24.57°)$ and $\mu_2 = \tan(36.5°)$; grain diameter $d = 4 \times 10^{-3}$ m; constant solids volume fraction $\phi^c = 0.56$; characteristic length $\mathcal{L} = 1.65 \times d$; and empirical constant $\beta = 0.135$. The value of $\hat{\nu}^g$ is chosen so that, after multiplication by the constant solids volume fraction $\phi^c = 0.56$, the coefficient entering the granular viscous term is $\phi^c\hat{\nu}^g \simeq 1.0 \times 10^{-4}$ $\mathrm{m}^{3/2}$ s^{-1}. This choice gives an effective granular viscosity of order 10^{-5} m^2 s^{-1} for a centimetre-scale grain layer, comparable to the prescribed fluid kinematic viscosity $\nu^f = 1 \times 10^{-5}$ m^2 s^{-1}. The remaining parameters are representative of the material properties used in the moving-bed flume experiments described in Davies (1990). The initial granular heap is formed by the collapse of a semicircular granular packing, with its longitudinal profile defined by

$$h^g(x,0) = \sqrt{r^2 - (x - x_0)^2}, \tag{46}$$

where $(x_0, 0)$ is the coordinate of the semicircle's center, and r is the radius. In this case, $x_0 = 1$ m, and the radius is defined as $r = \sqrt{2V_0/\pi}$, where V_0 corresponds to the initial granular and air volume per unit width. The morphology of the grain deposit that results from the collapse of the profile (Equation 46) is adopted as the initial grain thickness for the simulations.

4.2. Meng et al.'s (2022) Extended Model With Velocity Shear

The full system of Equations 8–17 are now solved numerically assuming a linear granular velocity profile with no basal slip and plug-flow in the fluid, that is, $\alpha^g = 0$, $m^g \to \infty$, and $\alpha^f = 1$. Substituting these values into the streamfunctions (Equation 22) implies that their difference

$$\psi^f(s) - \psi^g(s) = \bar{u}^f s - \bar{u}^g \frac{s^2}{h^g}. \tag{47}$$

It follows that in the undersaturated $\left(s = h^f\right)$ and oversaturated $(s = h^g)$ regimes

$$\psi^f - \psi^g = \begin{cases} \bar{u}^f h^f - \bar{u}^g \dfrac{\left(h^f\right)^2}{h^g}, & \text{undersaturated,} \\ h^g\left(\bar{u}^f - \bar{u}^g\right), & \text{oversaturated.} \end{cases} \tag{48}$$

The structure of the drag term therefore differs between the two regimes. In the oversaturated case, the expression is proportional to the depth-averaged velocity difference between the species $\bar{u}^f - \bar{u}^g$ and is therefore similar to classical depth-averaged models. However, it is not precisely the same, because it is multiplied by the granular thickness h^g rather than the full thickness of the flow. By contrast, in the undersaturated regime the term $\bar{u}^g\left(h^f\right)^2/h^g$ introduces a nonlinear dependence on the ratio of phase thickness. The interphase Darcy drag is therefore modulated not solely by the mean velocity difference, but also by the relative flow depths, reflecting the influence of differential shear between grains and fluid.

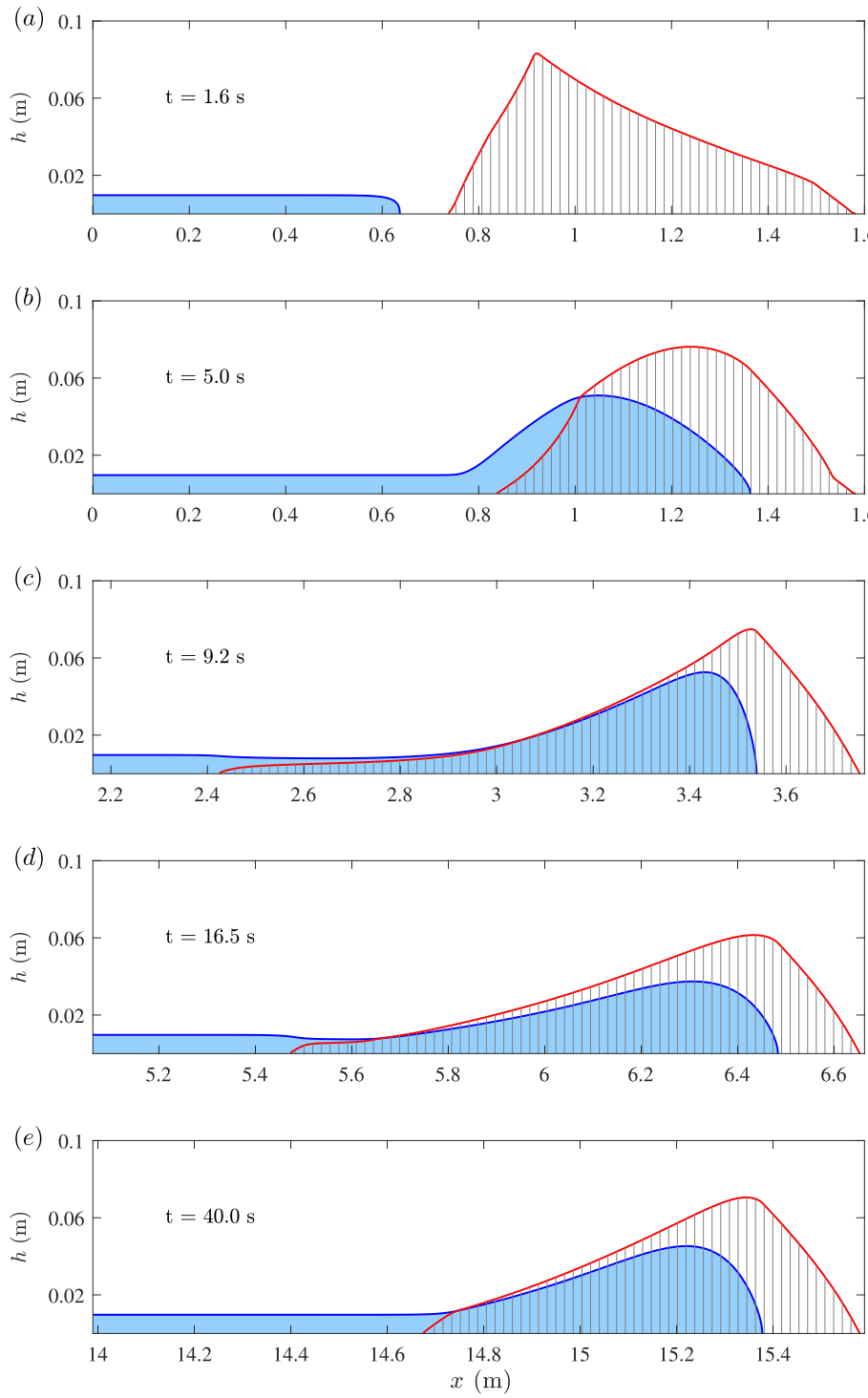


Figure 2. (a–e) Time-dependent simulation of Meng et al.'s (2022) model with spatial mesh resolution $\Delta x = 1 \times 10^{-4}$ m and velocity shear ($\alpha^g = 0$, $m^g \to \infty$, and $\alpha^f = 1$), showing the evolution of the grain depth h^g (red lines) and fluid depth h^f (blue lines) as an initially stationary pile of dry grains is infiltrated by the fluid and flows down a 15° slope. The fluid filled region is shaded blue and the granular region is hashed with black lines that are normal to the chute. An animation is included in Movie S1.

21699011, 2026, 10, Downloaded from https://agupubs.onlinelibrary.wiley.com/doi/10.1029/2025JF008556 by The University Of Manchester, Wiley Online Library on [18/10/2026]. See the Terms and Conditions (https://onlinelibrary.wiley.com/terms-and-conditions) on Wiley Online Library for rules of use; OA articles are governed by the applicable Creative Commons License

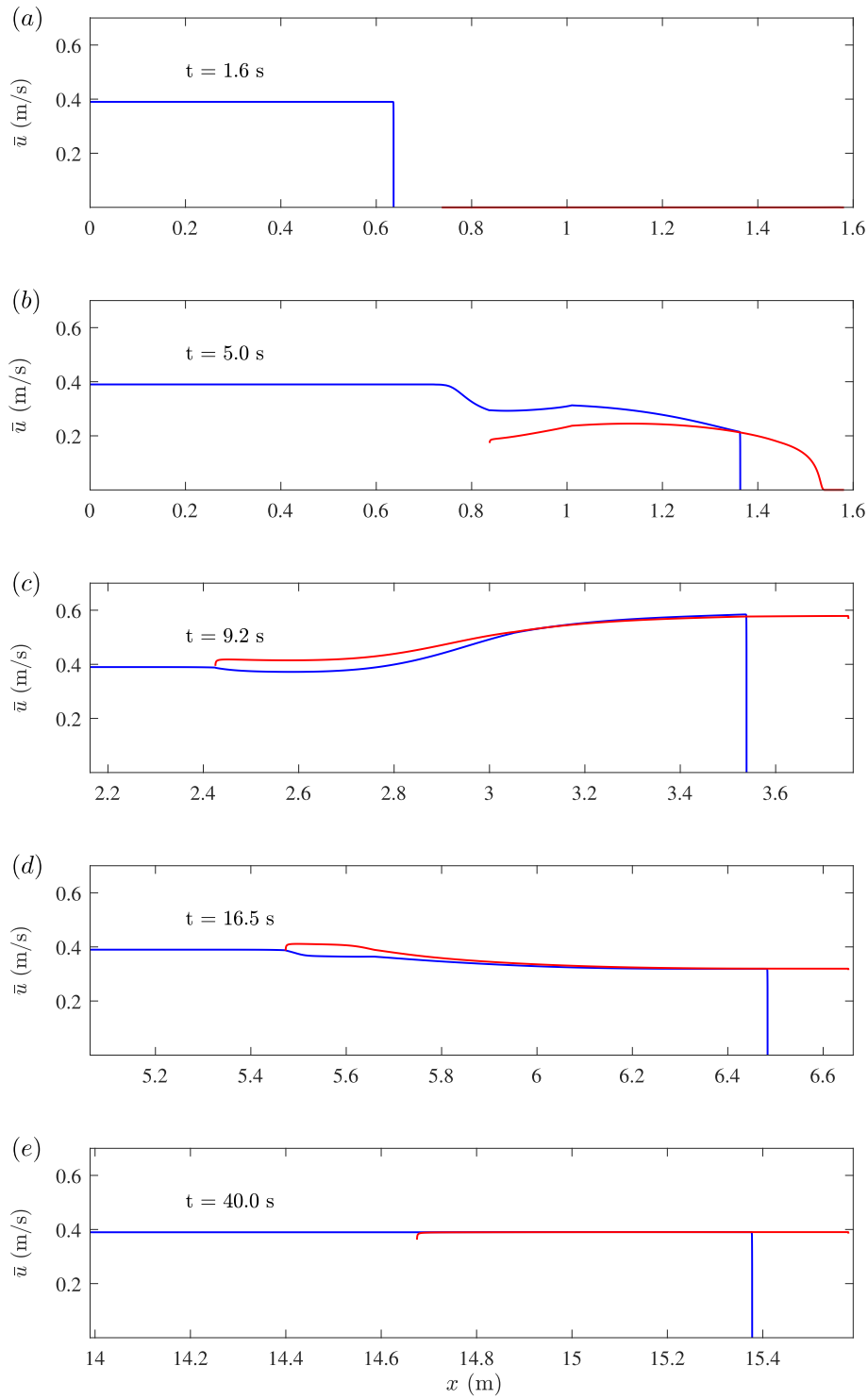


Figure 3. (a–e) Time-dependent simulations of Meng et al.'s (2022) model with spatial mesh resolution $\Delta x = 1 \times 10^{-4}$ m and velocity shear ($\alpha^g = 0, m^g \to \infty$, and $\alpha^f = 1$), showing the evolution of the depth-averaged granular velocity $\bar{u}^g$ (red lines) and the depth-averaged fluid velocity $\bar{u}^f$ (blue lines) as an initially stationary pile of dry grains is infiltrated by the fluid and flows down a 15° slope. An animation is included in Movie S2.

21699011, 2026, 10, Downloaded from https://agupubs.onlinelibrary.wiley.com/doi/10.1029/2025JF008556 by The University Of Manchester, Wiley Online Library on [18/10/2026]. See the Terms and Conditions (https://onlinelibrary.wiley.com/terms-and-conditions) on Wiley Online Library for rules of use; OA articles are governed by the applicable Creative Commons License

21699011, 2026, 10, Downloaded from https://agupubs.onlinelibrary.wiley.com/doi/10.1029/2025JF008556 by The University Of Manchester, Wiley Online Library on [18/10/2026]. See the Terms and Conditions (https://onlinelibrary.wiley.com/terms-and-conditions) on Wiley Online Library for rules of use; OA articles are governed by the applicable Creative Commons License

Figures 2 and 3 illustrate the transient evolution of flow heights and depth-averaged velocities for the extended Meng et al. (2022) model with velocity shear. At $t = 1.6$ s, a steady uniform fluid flow can be seen propagating downslope toward a stationary pile of particles, with volume $V_0 = 0.03467$ m^3 per unit width. As the fluid infiltrates through the particle pile (at $t = 5$ s), the fluid front increases significantly in height in order to overcome the seepage resistance imposed by the particles and an oversaturated region develops in the range $x \in [0.8, 1]$ m, which the numerical method is sufficiently robust to handle. At the same time, grains begin to move downslope due to (a) the fluid progressively reducing the basal friction in Equation 16 and (b) the Darcy drag in the saturated basal region pulling the grains downslope.

Under the influence of the granular pressure gradient, the grains accelerate downslope, and by $t = 9.2$ s, they exceed the inflow velocity of the fluid. At this stage, the depth-averaged velocity of the grains becomes nearly equal to that of the fluid phase in the undersaturated region. However, their local velocities differ significantly. In the lower saturated region of the flow, the fluid moves downslope faster than the grains, thereby driving the grains downslope. In contrast, in the upper dry region, velocity shear causes the dry surface layer to be transported downslope more rapidly than both the fluid and the grains in the lower saturated region.

As illustrated in Figure 2, the fluid thickness in the oversaturated tail of the flow is thinner than the inflow thickness at $t = 9.2$ s, resulting in increased basal friction acting on the fluid. Consequently, the depth-averaged velocity of the fluid in this region falls below the inflow velocity (see Figure 3c). The higher velocity in the main body of the flow, compared to the tail, leads to an elongation of the debris-flow body. As the flow continues to stretch, the associated pressure gradient gradually weakens. By $t = 16.5$ s, the forces acting on the dry granular front reach equilibrium; however, this equilibrium is not achieved in the undersaturated and oversaturated regions. Spatially, the pressure gradient diminishes progressively from the undersaturated region toward the fluid-rich tail, resulting in a gradual increase in the depth-averaged velocity of the grains.

As the depth-averaged velocity at the rear of the flow exceeds that of the main body, the debris flow begins to compress. This compression continues until a traveling wave develops at $t = 40$ s, at which point all depth-averaged velocities are equal to the inflow velocity, except for a small region in the granular tail. From this moment onward, the debris wave propagates at a constant speed. In the traveling reference frame, the shape of the debris wave therefore remains invariant. These transient evolution processes are vividly illustrated in Movies S1 and S2.

4.3. Ill-Posedness in the Absence of Viscous Terms

As discussed in Section 1, most depth-averaged multiphase debris-flow models suffer from resonances in the hyperbolic flux structure, which leads to short-wavelength instabilities and mathematical ill-posedness (Langham et al., 2025a, 2025b). In such regions of parameter space, infinitesimal perturbations grow without bound in the high-wavenumber limit and no convergent solution exists in the sense of Hadamard (Joseph & Saut, 1990). The fluid infiltration problem in Section 4.2 provides a perfect illustration of the effects of ill-posedness in the absence of the depth-averaged viscous terms in Equations 13 and 14.

Figure 4 and Movie S4 show the evolution of the inviscid solution computed on a fine mesh with $\Delta x = 2 \times 10^{-5}$ m. All other components of the model are unchanged compared to the computations in Section 4.2. During the initial stages of fluid infiltration into the static pile of grains, the solution appears smooth; however, short-wavelength oscillations emerge rapidly in the oversaturated regime at $t = 1.885$ s. These oscillations arise from the underlying ill-posed nature of the inviscid system in the oversaturated regime. By $t = 1.895$ s, the oscillations have spread spatially and contaminate an increasing portion of the oversaturated region. However, in the undersaturated regime the inviscid system is well-posed, and so as the fluid advances further downstream the ill-posed oscillations die off and both the fluid and grain free surface appear smooth again.

To explicitly demonstrate that the short-wavelength oscillations in the oversaturated regime are due to ill-posedness, it is necessary to perform a grid refinement study. Figures 5a–5c and Movies S3–S5 show a sequence of the inviscid simulations with increasingly fine grid resolution. Rather than converging toward a limiting solution as Δx decreases, the solution develops increasingly unstable and finer-scale oscillatory structures in the oversaturated regime. This is a typical signature of mathematical ill-posedness. This behavior arises because the numerical method is inherently diffusive, with a diffusivity that decreases with increasing grid resolution. For a relatively coarse mesh, such as in Figure 5a and Movie S3, the numerical viscosity is sufficiently

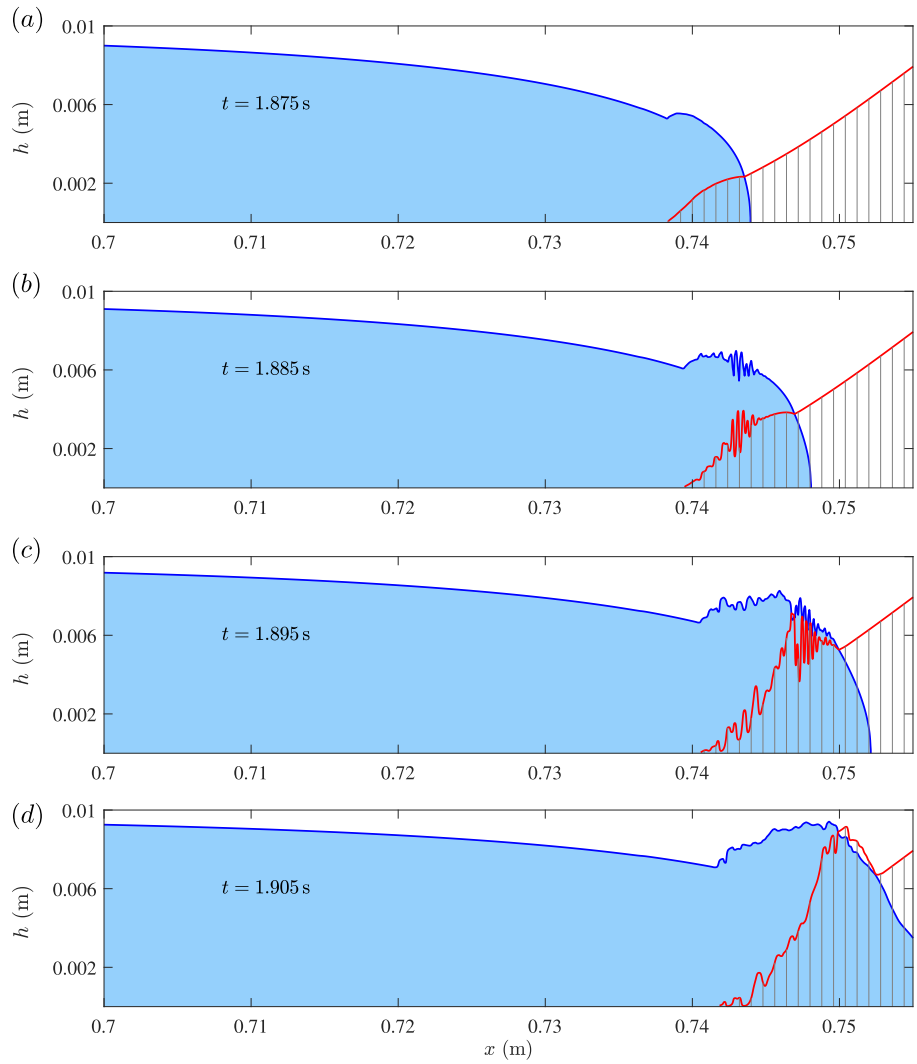


Figure 4. (a–d) Close up view of the granular depth h^g (red lines) and fluid depth h^f (blue lines) as the fluid first impinges on the grains using Meng et al.'s (2022) model without viscous regularization. The fluid filled region is shaded blue and the granular region is hashed with black lines that are normal to the chute. The simulation illustrates the emergence of short-wavelength instabilities associated with the ill-posedness and are computed with spatial mesh resolution $\Delta x = 2 \times 10^{-5}$ m. An animation is included in Movie S4.

large that it can suppress the ill-posed oscillations completely. However, as the level of numerical diffusion is progressively reduced, in Figures 5b and 5c and Movies S4 and S5, the grid-dependent instability becomes increasingly pronounced.

In contrast, when the viscous terms in Equations 13 and 14 are reinstated, the character of the solution changes fundamentally. As shown in Figure 5d and Movies S1, S6, and S7, simulations performed with different mesh resolutions approximately collapse onto a single curve as the grid is refined. The short-wavelength oscillations are suppressed and the solution exhibits clear grid convergence. The diagonal diffusion operator introduced through the granular and fluid viscosities ensures strictly positive diffusion coefficients in each momentum equation, thereby eliminating the unbounded high-wavenumber growth associated with resonant regions of the corresponding inviscid system. It is important to emphasize that the depth-averaged viscous contributions in Equations 13 and 14 are not simply introduced as an artificial numerical regularization, but they represent important additional constitutive behavior of the grains and the fluid. Indeed, their functional form and parametric dependence can be derived from non-depth-averaged constitutive laws (GDR-MiDi, 2004; Gray & Edwards, 2014; Jop et al., 2006).

21699011, 2026, 10, Downloaded from https://agupubs.onlinelibrary.wiley.com/doi/10.1029/2025JF008556 by The University Of Manchester, Wiley Online Library on [18/10/2026]. See the Terms and Conditions (https://onlinelibrary.wiley.com/terms-and-conditions) on Wiley Online Library for rules of use; OA articles are governed by the applicable Creative Commons License

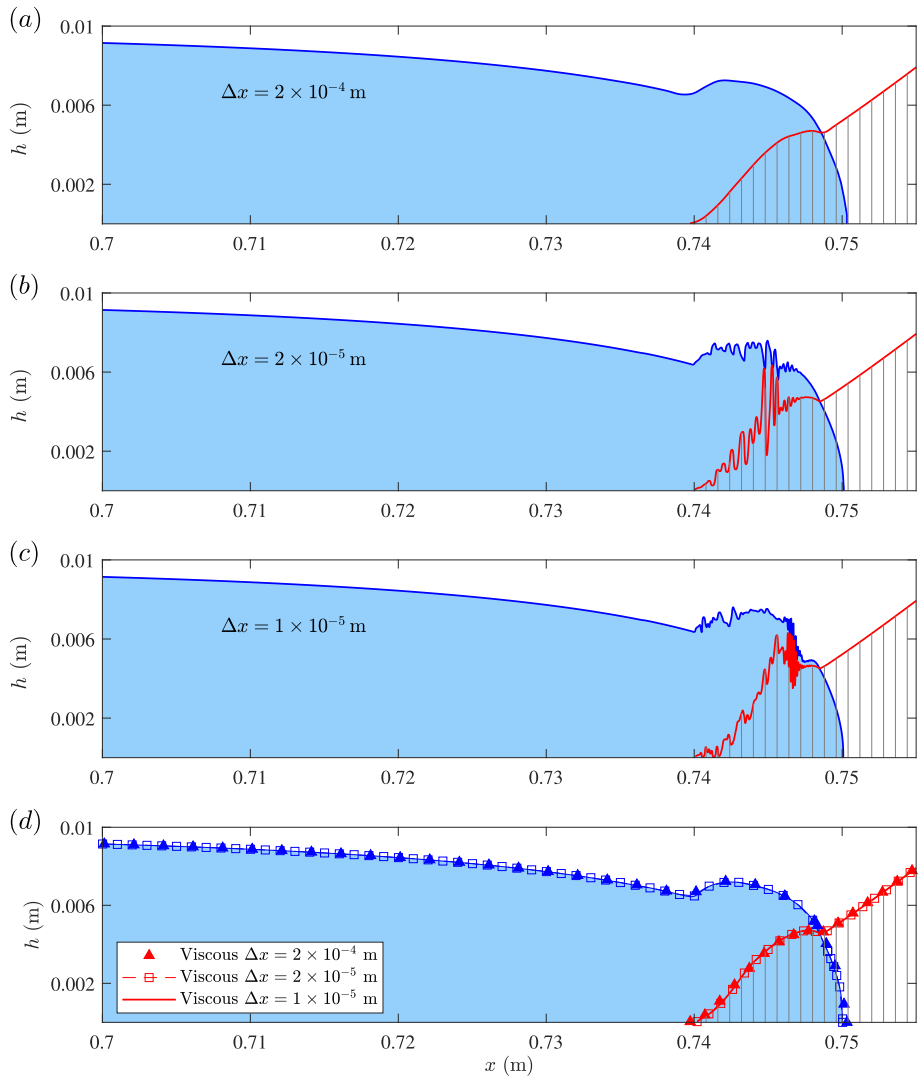


Figure 5. Close up view of the granular depth h^g (red lines) and fluid depth h^f (blue lines) as the fluid first impinges on the grains using Meng et al.'s (2022) model at $t = 1.89$ s under different spatial resolutions. Panels (a–c) show results obtained without viscous regularization for $\Delta x = 2 \times 10^{-4}$, 2×10^{-5} and 1×10^{-5} m, respectively, while panel (d) shows the grid convergence of the full viscously regularized model for the same grid resolutions. Movies S3–S5 show animations of each of the ill-posed simulations, while Movies S1, S6, and S7 show grid-converged animations of the full viscous simulations.

4.4. Comparison of the Computed and Traveling Wave Solutions

As a further test of the numerical method a traveling-wave solution is constructed to compare against the numerical solution computed in Section 4.2. A moving reference frame is introduced, traveling downslope at the same speed, u_0, as the inflow. The variables in the moving framework are related to those in the fixed system by

$$\xi = x - u_0 t, \qquad \tau = t. \tag{49}$$

The steady-state mass balance equations for grains and fluid in the traveling frame are

$$\frac{\mathrm{d}}{\mathrm{d}\xi}\left(h^g \phi^c (\bar{u}^g - u_0)\right) = 0, \tag{50}$$

$$\frac{\mathrm{d}}{\mathrm{d}\xi}\left(h^f (1 - \phi^c \mathcal{H}) (\bar{u}^f - u_0)\right) = 0. \tag{51}$$

21699011, 2026, 10, Downloaded from https://agupubs.onlinelibrary.wiley.com/doi/10.1029/2025JF008556 by The University Of Manchester, Wiley Online Library on [18/10/2026]. See the Terms and Conditions (https://onlinelibrary.wiley.com/terms-and-conditions) on Wiley Online Library for rules of use; OA articles are governed by the applicable Creative Commons License

Integrating these subject to the boundary conditions $h^g = 0$ and $h^f = 0$ at the grain and fluid fronts, respectively, yields

$$h^g \phi^c (\bar{u}^g - u_0) = 0, \qquad \text{and} \qquad h^f (1 - \phi^c \mathcal{H}) (\bar{u}^f - u_0) = 0, \tag{52a, b}$$

which are satisfied when either $h^g = 0$ and $h^f = 0$, or the velocities are identical

$$\bar{u}^g = \bar{u}^f = u_0. \tag{53}$$

The fact that the phase velocities are spatially uniform implies that the depth-averaged viscous contributions in Equations 13 and 14 vanish. Consequently, in the traveling steady state, the extended system (Equation 8–17) reduces to the inviscid model employed by Meng et al. (2022) to quantitatively capture the steady-state behavior observed in Davies's (1990) moving-bed-flume experiments. Substituting the velocity condition (Equation 53), the streamfunction difference (Equation 48) and the Chézy formula (Equation 34) into the grain and fluid momentum balance Equations 9 and 11, Meng et al. (2022) derived a pair of ordinary differential equations (ODEs) for h^g and h^f in the undersaturated regime

$$\frac{\mathrm{d}h^g}{\mathrm{d}\xi} = \tan\zeta - \mu^b \left(1 - \gamma \frac{h^f}{h^g}\right) + \frac{C^d u_0}{\varrho^{g\star} \phi^c g \cos\zeta} \left(\frac{h^f}{h^g}\right) \left(1 - \frac{h^f}{h^g}\right), \tag{54}$$

$$\frac{\mathrm{d}h^f}{\mathrm{d}\xi} = \tan\zeta - \frac{n^2 u_0^2}{\left(h^f\right)^{4/3} \cos\zeta} - \frac{C^d u_0}{\varrho^{f\star} (1 - \phi^c) g \cos\zeta} \left(1 - \frac{h^f}{h^g}\right), \tag{55}$$

as well as in the oversaturated regime

$$\frac{\mathrm{d}h^g}{\mathrm{d}\xi} = \tan\zeta - \mu^b + \left(\frac{\gamma}{1-\gamma}\right) \frac{n^2 u_0^2}{\left(h^f\right)^{4/3} \cos\zeta}, \tag{56}$$

$$\frac{\mathrm{d}h^f}{\mathrm{d}\xi} = \tan\zeta - \frac{n^2 u_0^2}{\left(h^f\right)^{4/3} \cos\zeta}. \tag{57}$$

The ODEs (Equations 54 and 55) are integrated backwards from the grain and fluid fronts, $\xi = \xi^g$ and $\xi = \xi^f$, respectively, where $\xi^f < \xi^g$, until the condition $h^g = h^f$ is satisfied. This integration is performed using Matlab's `ode45` solver for initial value problems. The initial conditions correspond to the vanishing thickness at the flow fronts, that is, $h^g = 0$ at $\xi = \xi^g$ and $h^f = 0$ at $\xi = \xi^f$. At the fluid front $\left(h^f = 0\right)$, a singularity arises, due to the fluid friction, in which the gradient of the fluid thickness balances the fluid basal friction. This balance is used to determine the shape of the fluid free surface near the fluid front (Meng et al., 2022). At the transition point between the undersaturated and oversaturated regimes, the flow thicknesses are equal, $h^f = h^g$, resulting in the disappearance of the Darcy interaction drag in the undersaturated equations. Moving backwards from this transition point, the ODEs (Equations 56 and 57), which also do not depend of the Darcy drag terms, are integrated until h^g reaches zero. At this point, the fluid thickness slightly exceeds the inflow thickness. Since $h^g = 0$ is a trivial solution of Equation 9, the underlying system degenerates to a single ODE (Equation 57), which determines the shape of the pure fluid regime.

The dry snout length, $\xi^g - \xi^f$, is determined implicitly by iterating until the solution has the grain volume specified in the experiment. Figure 6a shows a comparison between the traveling-wave solution, constructed with $\xi^g - \xi^f = 0.202$ m, and the numerical traveling wave solution for $V_0 = 0.03467$ m^3 per unit width, shown in Figure 2 at $t = 40$ s. The numerical solution is shifted so that the grain front is positioned at $\xi = 0$. It is in excellent agreement with the exact traveling wave solution, which confirms the accuracy of the numerical method in handling both the non-conservative and diffusive terms. A second case involving a smaller grain volume is also tested to further verify the accuracy and robustness of the numerical approach. As shown in

21699011, 2026, 10, Downloaded from https://agupubs.onlinelibrary.wiley.com/doi/10.1029/2025JF008556 by The University Of Manchester, Wiley Online Library on [18/10/2026]. See the Terms and Conditions (https://onlinelibrary.wiley.com/terms-and-conditions) on Wiley Online Library for rules of use; OA articles are governed by the applicable Creative Commons License

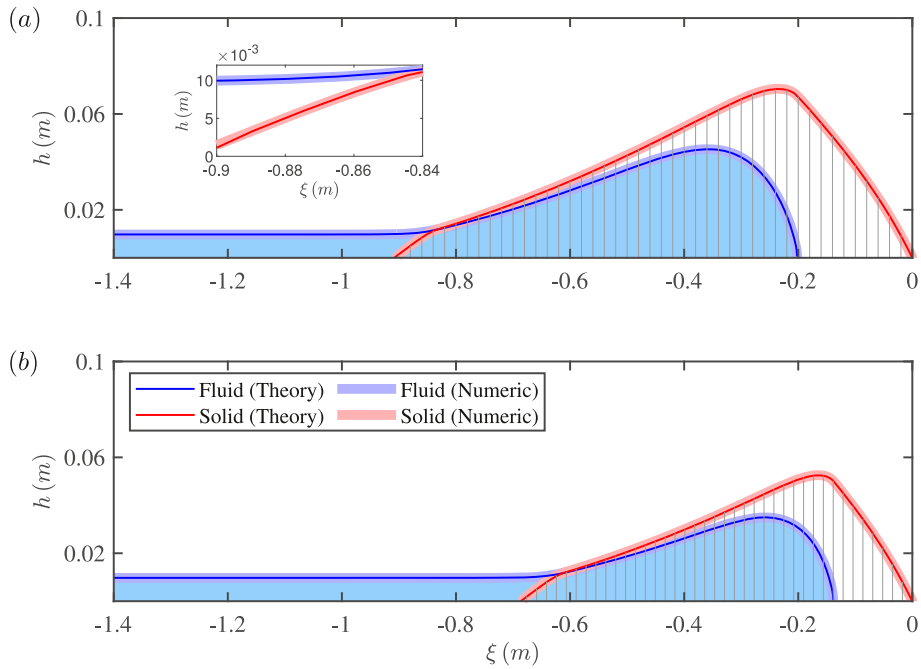


Figure 6. Exact traveling wave solutions to Meng et al.'s (2022) extended theory for the grain and fluid depths (thin red and blue solid lines) and corresponding numerical solutions (thicker lighter red and blue solid lines) for granular volumes of (a) $V_0 = 0.03467$ m^3 and (b) $V_0 = 0.0198$ m^3 per unit width. The flow is driven downslope by a steady uniform fluid flow of depth of 9.7 mm and speed 0.39 m/s. Note, the numerical solution is shifted so that the grain front is positioned at $\xi = 0$ to allow a direct comparison.

Figure 6b, the steady-traveling numerical solution aligns closely with the traveling-wave solution constructed with $\xi^g - \xi^f = 0.13867$ m.

Meng et al. (2022) showed that the traveling wave solution can quantitatively capture the steady-state granular free-surface shape and particle recirculation observed in Davies's (1990) moving-bed-flume experiments. The simulations, in Figures 2 and 3 and Movies S1 and S2, therefore show how a static pile of grains can be infiltrated and mobilized by a fluid to form a steadily traveling wave, with a thick dry front and increasingly fluid-rich tail.

4.5. Meng et al.'s (2022) Extended Model With Plug Flow Profiles

To contrast against the solutions with velocity shear, it is instructive to solve the full system assuming plug-flow in the grains and the fluid, that is, $\alpha^g = 1$ and $\alpha^f = 1$. It is important to stress that this is still Meng et al.'s (2022) extended model, but with plug flow profiles; the rest of the system (Equations 8–17) is unchanged. In this case, Equation 22 implies that the streamfunction difference

$$\psi^f - \psi^g = s\left(\bar{u}^f - \bar{u}^g\right), \tag{58}$$

where recall s is the internal interface height. This type of depth-averaged Darcy drag term is linearly proportional to the depth-averaged velocity difference between the species, which is akin to standard two-phase debris flow models (see, e.g., Bouchut et al., 2016; Iverson & George, 2014; Meng & Wang, 2018; Pelanti et al., 2008; Pitman & Le, 2005; Pudasaini, 2012). Although the assumption in Equation 58 only looks like a marginal change to Equation 47, it makes a huge difference to the solutions.

Figures 7 and 8 show the transient evolution as fluid infiltrates a static pile of grains when there is no shear. At $t = 1.6$ s, when the grains and the fluid are completely separated from one another, the solution is exactly the same as the case with shear in Figures 2a and 3a. The differences between the two models begin to appear as soon as the grains and fluid interpenetrate. At $t = 5$ s the fluid has penetrated further forward for plug flow, and is moving faster than the grains throughout the entire fluid infiltrated region. In contrast, for shear flow, the fluid

21699011, 2026, 10, Downloaded from https://agupubs.onlinelibrary.wiley.com/doi/10.1029/2025JF008556 by The University Of Manchester, Wiley Online Library on [18/10/2026]. See the Terms and Conditions (https://onlinelibrary.wiley.com/terms-and-conditions) on Wiley Online Library for rules of use; OA articles are governed by the applicable Creative Commons License

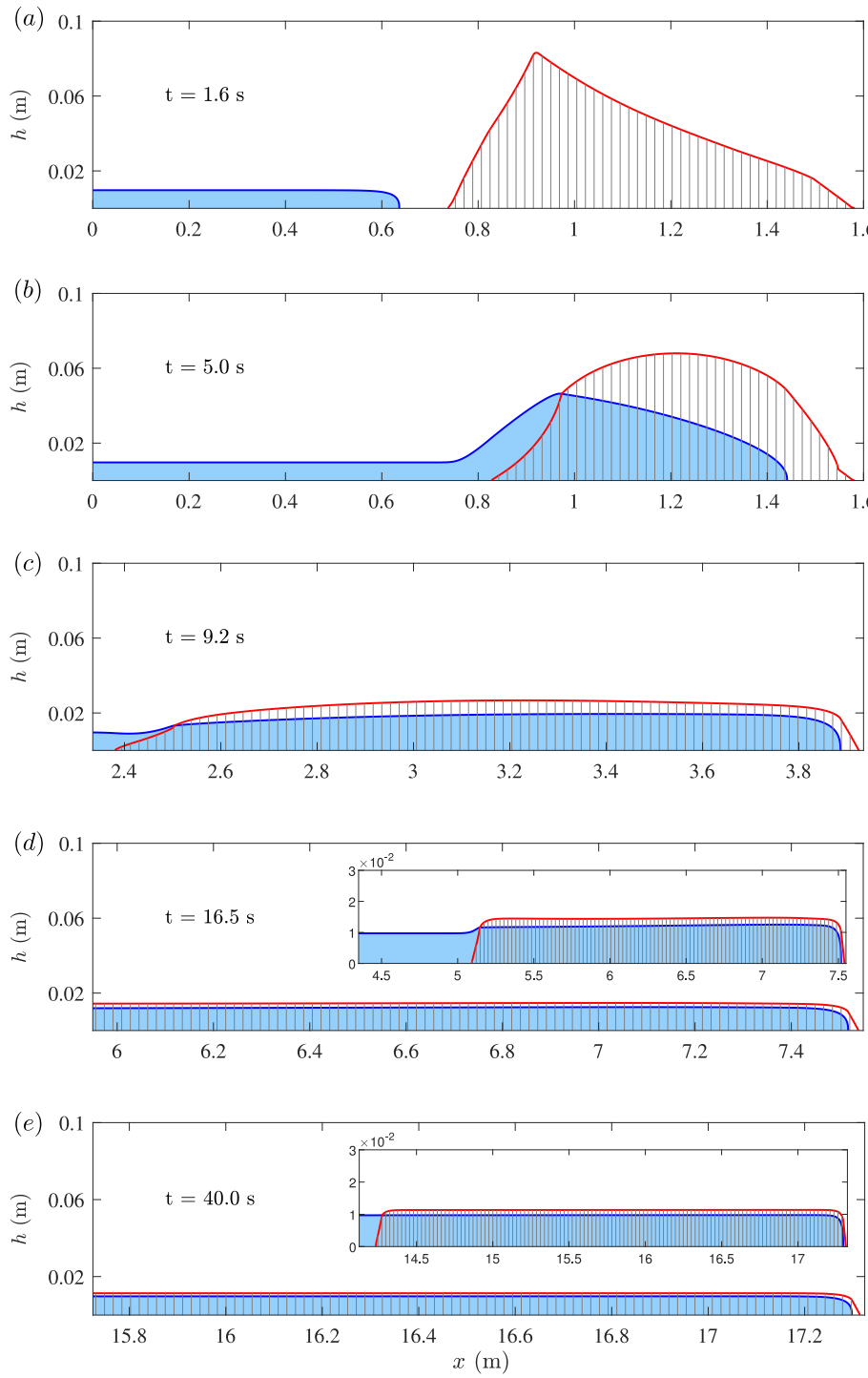


Figure 7. (a–e) Time-dependent simulation of Meng et al.'s (2022) model with spatial mesh resolution $\Delta x = 1 \times 10^{-4}$ m and plug flow profiles, showing the evolution of the grain depth h^g (red lines) and fluid depth h^f (blue lines) as an initially stationary pile of dry grains is infiltrated by fluid and flows down a 15° slope ($\alpha^g = 1$ and $\alpha^f = 1$). The fluid filled region is shaded blue and the granular region is hashed with black lines that are normal to the chute. (d, e) The complete granular domain is shown in the inset. An animation is included in Movie S8.

21699011, 2026, 10, Downloaded from https://agupubs.onlinelibrary.wiley.com/doi/10.1029/2025JF008556 by The University Of Manchester, Wiley Online Library on [18/10/2026]. See the Terms and Conditions (https://onlinelibrary.wiley.com/terms-and-conditions) on Wiley Online Library for rules of use; OA articles are governed by the applicable Creative Commons License

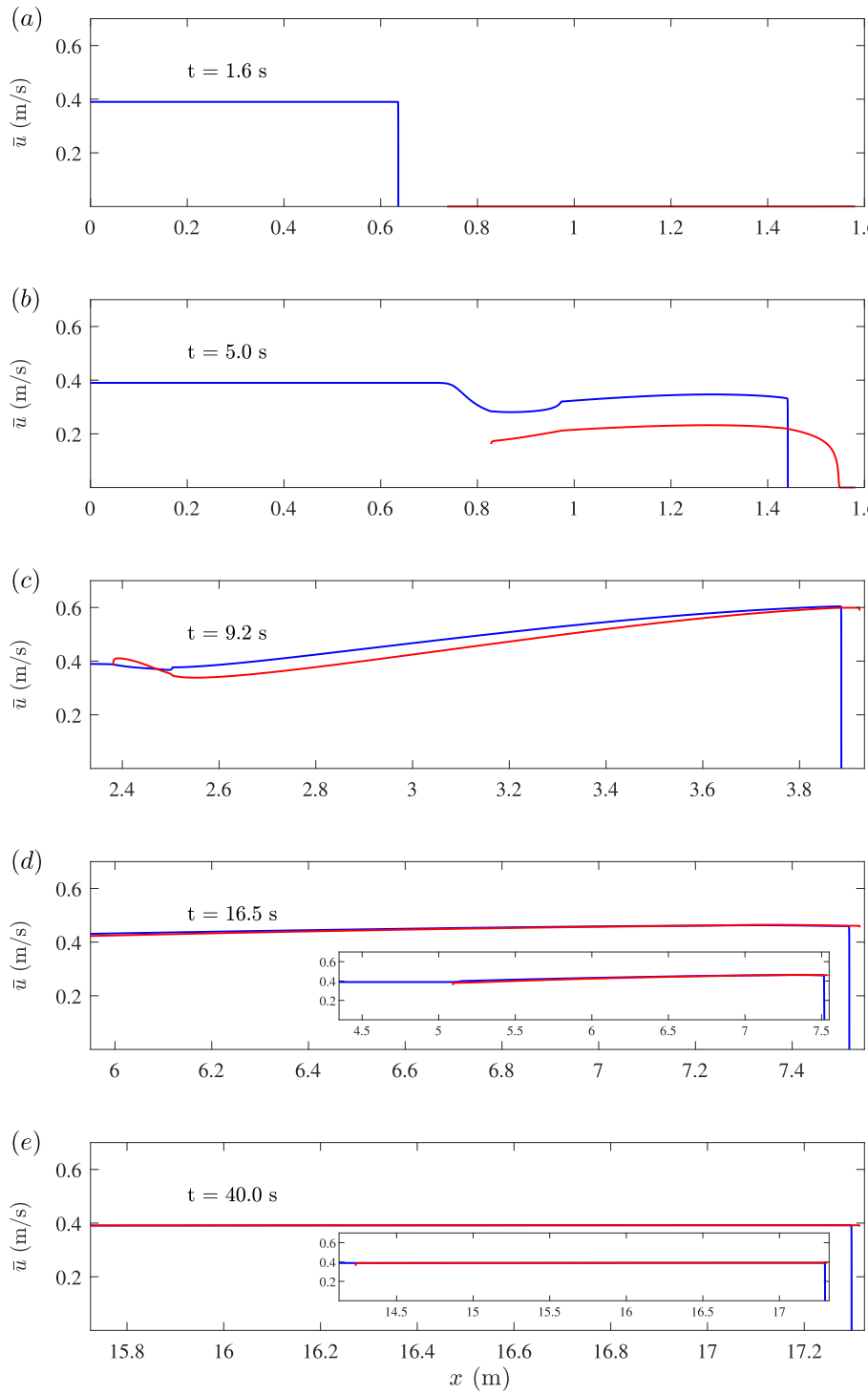


Figure 8. (a–e) Time-dependent simulation of Meng et al.'s (2022) model with spatial mesh resolution $\Delta x = 1 \times 10^{-4}$ m and plug flow profiles, showing the evolution of the depth-averaged granular velocity $\bar{u}^g$ (red lines) and the depth-averaged fluid velocity $\bar{u}^f$ (blue lines) as an initially stationary pile of dry grains is infiltrated by fluid and flows down a 15° slope ($\alpha^g = 1$ and $\alpha^f = 1$). (d, e) The complete granular domain is shown in the inset. An animation is included in Movie S9.

velocity progressively reduces to the grain velocity as the fluid front is approached (see Figures 3b and 8b). The increased infiltration of the fluid, in the absence of shear, implies that the basal granular friction is reduced by buoyancy sooner and the grains can start moving downslope more easily. While the oversaturated tail of the pile

21699011, 2026, 10, Downloaded from https://agupubs.onlinelibrary.wiley.com/doi/10.1029/2025JF008556 by The University Of Manchester, Wiley Online Library on [18/10/2026]. See the Terms and Conditions (https://onlinelibrary.wiley.com/terms-and-conditions) on Wiley Online Library for rules of use; OA articles are governed by the applicable Creative Commons License

21699011, 2026, 10, Downloaded from https://agupubs.onlinelibrary.wiley.com/doi/10.1029/2025JF008556 by The University Of Manchester, Wiley Online Library on [18/10/2026]. See the Terms and Conditions (https://onlinelibrary.wiley.com/terms-and-conditions) on Wiley Online Library for rules of use; OA articles are governed by the applicable Creative Commons License

and the pure fluid region are virtually identical in both cases, the reduced granular friction with a plug profile allows the pile to collapse more easily and advance slightly further downslope than in the case of shear.

By $t = 9.2$ s, the fluid is able to penetrate almost to the very front, which is much further downstream and consequently the flow is much thinner than in the case of shear. Indeed, by $t = 16.5$ s, the stretching is so great that the body of grains no longer fits into Figure 7d, but has to be shown in a spatially compressed inset image. The fact that only a very small dry front is formed implies that the downstream velocity remains fastest at the front and the flow continues to stretch until the solution locks onto a steady-traveling flow state at approximately $t = 40$ s when the velocities of the grains and the fluid equilibrate. The solution consists of (i) a tiny dry front that is connected to (ii) a large undersaturated region with uniform grain and fluid depth, and (iii) a short oversaturated transition to (iv) a pure-fluid tail (see Figures 7e and 8e). The apparently minor modification to the form of the depth-integrated Darcy drag from Equation 47 to Equation 58 has a very profound effect on the solution. In particular, for the same steady-state wave speed u_0, velocity shear allows a large amplitude dry front to form that has much more destructive potential than the low amplitude elongated steady-state solution for plug flow. However, the much increased spreading for plug flow also generates higher transient velocities, which could also make such flows more destructive.

The shear-resolved solutions shown in Figures 2 and 3 exhibit traveling-wave structures and phase-separation patterns consistent with those reported in Davies (1990). However, there may be situations where the stretching solutions such as the ones shown in Figures 7 and 8 may also be physically realistic (see, e.g., Aaron et al., 2025; Wetter et al., 2026). Meng et al.'s (2022) model therefore has the capacity to encompass both cases within a single framework, but care needs to be taken to make accurate assumptions about the downslope granular and fluid velocity profiles through the flow depth as well as the permeability of the grain matrix. It is worth noting that both cases lead to different forms of phase separation that cannot be represented with a composite model such as the one derived in Section 2.2.

5. Inclined Flow and Runout Dynamics of Granular-Fluid Avalanches

The three variants of Meng et al.'s (2022) extended model are now used to show the effect of increasing the complexity of the physics in simulating the large-scale experiments of Taylor-Noonan et al. (2022).

5.1. Model Parameters, and Initial and Boundary Conditions

Meng et al. (2024) also simulated Taylor-Noonan et al.'s (2022) experiments, but using a modified system of conservative equations that were appropriate for dominantly undersaturated flows. The results in this paper use exactly the same parameters, and initial and boundary conditions, so that direct comparisons can be drawn. The experimental geometry is illustrated in Figure 1. It consists of an inclined section that is abruptly connected to a flat runout plane. When using terrain-following coordinates sharp transitions are not permitted, as they may result in artificial overlap of the solution domain. To mitigate this, the slope is assumed to have rapid smooth transition in the slope angle

$$\zeta(x) = \begin{cases} \zeta_0, & 0 \le x \le x_a, \\ \zeta_0\left(1 - 3\eta^2 + 2\eta^3\right), & x_a \le x \le x_b, \\ 0, & x_b \le x, \end{cases} \tag{59}$$

where $\eta = (x - x_a)/(x_b - x_a)$ and the parameters are summarized in Table 1. Although the coefficients in the basal granular friction law (Equation 30) were not measured by Taylor-Noonan et al. (2022), Meng et al. (2024) calibrated them by matching the experimental dry run-out distances, with different release volumes, to simulations. These coefficients along with the intrinsic density of the grains $\varrho^{g\star}$, the intrinsic density of the fluid $\varrho^{f\star}$, the grain viscosity coefficient $\hat{\nu}^g$, the fluid dynamic viscosity μ^f, the Manning coefficient n and representative flowing solids volume fraction are summarized in Table 1. Moderate variations of ϕ^c within its admissible range do not affect the qualitative flow dynamics.

21699011, 2026, 10, Downloaded from https://agupubs.onlinelibrary.wiley.com/doi/10.1029/2025JF008556 by The University Of Manchester, Wiley Online Library on [18/10/2026]. See the Terms and Conditions (https://onlinelibrary.wiley.com/terms-and-conditions) on Wiley Online Library for rules of use; OA articles are governed by the applicable Creative Commons License

Table 1
Physical Parameters Measured in the Experiments and Used in the Computations in Section 5

Parameter	Measured values	Model values
Position of the gate	–	3.14 m
Position of the start of the slope break, x_a	–	9.87 m
Position of the end of the slope break, x_b	–	10.27 m
Diameter, d	3.85 mm	3.85 mm
Chute angle, ζ_0	30°	30°
Minimum friction angle ζ_1	–	22.2°
Maximum friction angle ζ_2	–	25.6°
Frictional length scale $\mathcal{L}$	–	$1.65 \times d$
Dimensionless empirical constant β	–	0.135
Solid density, $\varrho^{g\star}$	2,241 kg m^{-3}	2,241 kg m^{-3}
Fluid density, $\varrho^{f\star}$	Tap water	1,000 kg m^{-3}
Grain viscosity coefficient, $\dot{\nu}^g$	–	1.79×10^{-4} m$^{\frac{3}{2}}$ s^{-1}
Fluid dynamic viscosity, μ^f	Tap water	0.001 Pa s
Fluid kinematic viscosity, ν^f	Tap water	1×10^{-5} m^2 s^{-1}
Manning coefficient, n	–	0.016 s m$^{-\frac{1}{3}}$
Initial solids volume fraction, ϕ^g_{ini}	–	0.585
Flowing solids volume fraction, ϕ^c	–	0.48

In Taylor-Noonan et al.'s (2022) experiments, the grains are initially packed behind a gate and saturated with water. Since the static grains have a solids volume fraction ϕ^g_{ini} the fluid occupies a volume fraction $1 - \phi^g_{\text{ini}}$. However, once the grains are released their flowing solids volume fraction ϕ^c is less than ϕ^g_{ini}. Meng et al.'s (2022) theory assumes that ϕ^c is constant and it is not possible to explicitly account for the initial volume fraction decrease on release. Instead, the initial condition is modified as illustrated in the inset of Figure 1, by expanding the grains height normal to the chute and allowing the fluid to sink down into the expanded grain matrix. The same procedure is used here to modify the initial condition, and it is described in detail in Meng et al. (2024).

The computational domain extends 20 m from the origin $x = 0$ m. It is discretized using 4,667 grid points, corresponding to a uniform spatial resolution of $\Delta x = 0.0043$ m. This resolution is sufficient to obtain grid-converged numerical solutions. At the boundary of the computational domain, zero gradient conditions are applied to all fields. However, the extent of the domain is chosen so that no material ever reaches the boundary.

5.2. Simulations Using the Composite Debris-Flow Model of Section 2.2

Simulations using the composite debris-flow model derived in Section 2.2 are shown in Figure 9 and Movie S10 for a release volume of 0.383 m^3/m of fluid-saturated grains per unit width. Note that since Taylor-Noonan et al.'s (2022) flume is 2.09 m wide this is equivalent to an experimental release of 0.8 m^3. Unlike the subsequent simulations with Meng et al.'s (2022) extended two-phase model, the initial saturated configuration is not modified to account for the volume expansion during flow. Instead, the solids volume fraction

$$\phi^c = \phi^g_{\text{ini}} = 0.585, \tag{60}$$

is assumed, and fluid occupies the entire pore space, consistent with the model assumptions. This complete saturation reduces the granular friction by the maximum amount, so one might anticipate that the flow would be highly mobile. However, the source term (Equation 28) in the composite debris-flow model implies that both the granular and fluid drag act simultaneously on the body. Although the granular friction is low, the quadratic

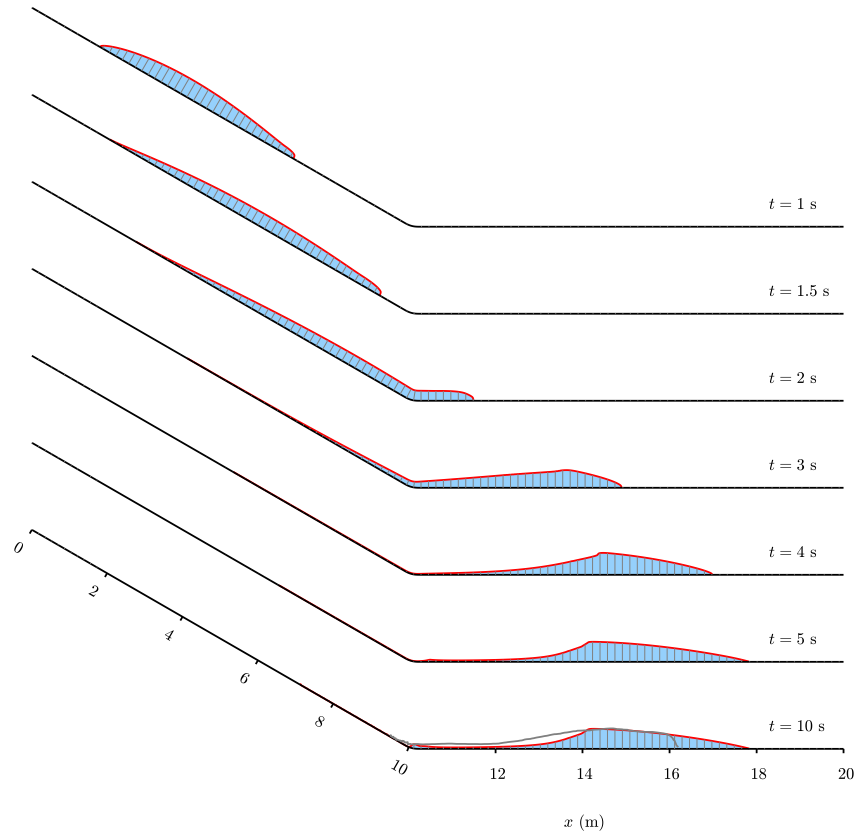


Figure 9. Computed temporal and spatial evolution of the composite debris-flow model after 0.383 m^3/m of fluid-saturated grains are released down Taylor-Noonan et al.'s (2022) flume. This model (derived in Section 2.2) assumes that there is no phase separation and the grain and fluid free surfaces are identical (red line). Since the flow is thin, the flow thickness is multiplied by a factor of four and projected normally to the chute along the straight gray lines to aid visualization. The region occupied by the fluid and grains is shaded blue. The gray solid line at $t = 10$ s shows the measured experimental deposit for comparison. Movie S10 shows an animation of the simulation.

velocity dependence in the fluid friction prevents it from attaining high speeds. As a result, as the body accelerates downslope and spreads out through the gradients of the depth-averaged pressure, it does not travel that fast and the front only reaches the runout plane at approximately 1.7 s. Here it slows down, but since the granular friction is low it is able to travel a long distance before it finally stops.

In Figure 9, the final experimental deposit is shown at $t = 10$ s for comparison. From this, it is clear that the computed front is approximately 1.6 m further downstream and the tail is considerably thinner than in the experiment. To quantify the runout, the front position, the position of the center of mass (CoM) and the approximate position of the tail are extracted from the computational results and plotted in Figure 10 for the range of experimental release volumes investigated by Taylor-Noonan et al. (2022). In the experiments, some particles stick to the inclined section of the chute due to surface tension, so not all the mass reaches the runout plane. To account for this, the approximate tail position x_{tail} is defined using a mass-based criterion. Specifically, x_{tail} is defined as the location on the run-out plane satisfying

$$\frac{\int_{x_{\text{tail}}}^{x_f} h^g_{\text{dep}} dx}{\int_{x_0}^{x_f} h^g_{\text{dep}} dx} = 0.98, \tag{61}$$

where x_f denotes the front position, x_0 the upstream boundary of the deposited mass, and $h^g_{\text{dep}}(x)$ the granular deposit thickness. Under the assumption of spatially uniform density, deposited mass is proportional to deposit volume, so this corresponds to a 98% mass criterion. Figure 10a shows that the predicted tail position is in very

21699011, 2026, 10, Downloaded from https://agupubs.onlinelibrary.wiley.com/doi/10.1029/2025JF008556 by The University Of Manchester, Wiley Online Library on [18/10/2026]. See the Terms and Conditions (https://onlinelibrary.wiley.com/terms-and-conditions) on Wiley Online Library for rules of use; OA articles are governed by the applicable Creative Commons License

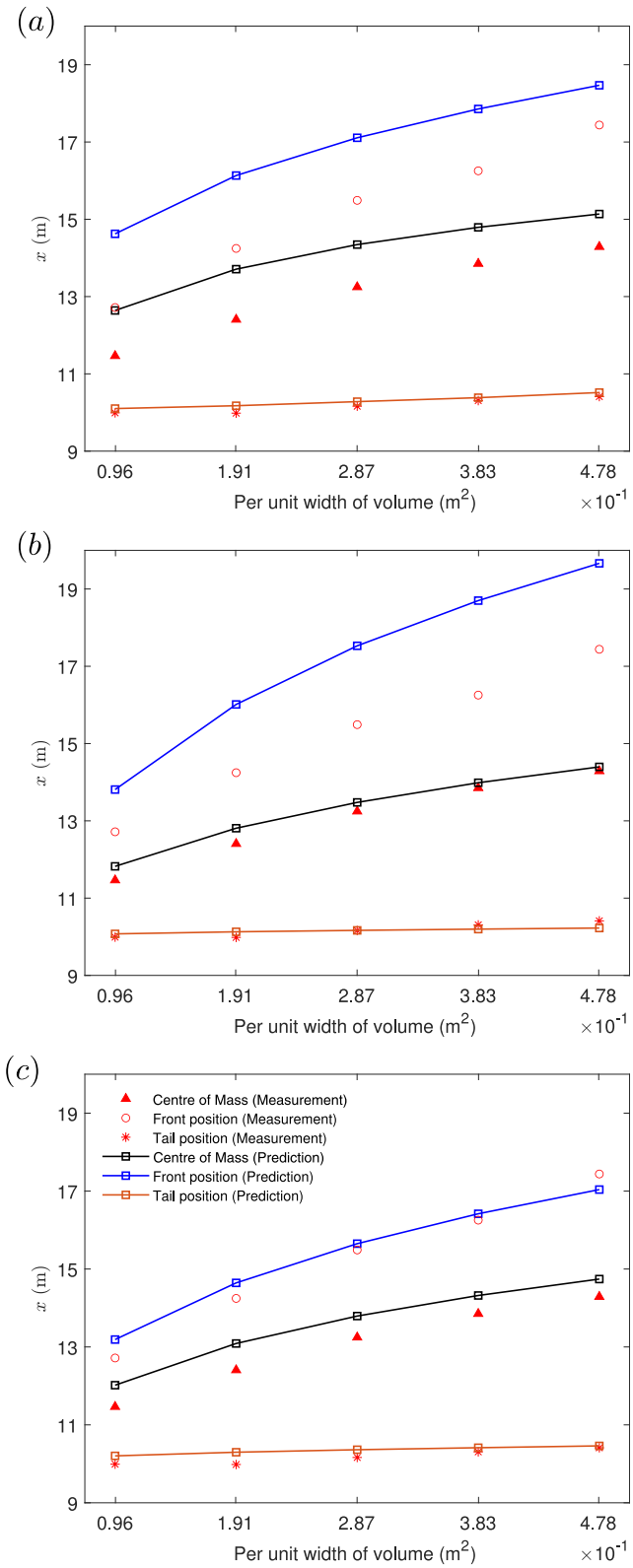


Figure 10.

good quantitative agreement with the experimental results for the whole range of release volumes. However, the predicted CoM position and the front position lie consistently ahead of the experimental results. This is surprising because it will now be shown that the composite debris-flow model moves slower than both the two-phase models on the inclined section of the chute. As mentioned above, this is due to the composite source term (Equation 28) which simultaneously minimizes granular friction and penalizes rapid motion.

5.3. Simulations Using Extended Meng et al. (2022) With Plug Flow

The simulation results for Meng et al.'s (2022) extended model assuming plug flow in both the grains and the fluid, that is,

$$\alpha^g = 1, \quad \alpha^f = 1, \tag{62}$$

are shown in Figure 11 and Movie S11 for a release volume of 0.383 m^3/m of fluid-saturated grains per unit width. This simulation is directly comparable with that in Figure 12 of Meng et al. (2024). Within the main body the granular friction is reduced by the presence of the fluid, so the grains are able to accelerate rapidly downslope, together with the fluid, and spread under the influence of the granular and fluid pressure gradients. The spreading is similar to the fluid infiltration problem on the inclined plane in Figures 7 and 8. The singular nature of the fluid drag law as $h^f \to 0$ implies that an infinite gradient has to build up at the fluid front before it can move downslope. This leads to relative motion between the grains and the fluid close to the front, and a small dry front is generated that is followed by a small oversaturated region immediately behind it. Due to the initial conditions and expansion of the grain matrix, most of the flow is, however, undersaturated.

The front of the avalanche reaches the runout plane at approximately 1.4 s, which is much sooner than the composite debris-flow model. Once on the runout plane, the granular friction remains low and the flow is able to propagate easily out over it with the front coming to rest close to the 18.5 m mark at about $t = 5$ s, with some slow drainage of fluid out of the front thereafter. The multiphase model with the plug flow assumption therefore has a significantly longer runout than the composite debris-flow model. This is somewhat unexpected as the expansion of the initial grain matrix implies the buoyancy reduction of the granular friction is smaller, that is, the effective granular friction is larger. However, unlike the composite debris-flow model the fluid friction does not appear explicitly in the granular momentum balance, and only acts indirectly via the Darcy drag coupling.

At $t = 5$ s, the thin tail (shown in the inset image) is still undersaturated and slowly drains off the chute, eventually breaking up into waves. Overall, the simulation is almost identical to that obtained using the modified conservative

Figure 10. A comparison between the predicted front (blue), center of mass (black), and approximate tail (red) positions against experiments (symbols) for the range of release volumes investigated by Taylor-Noonan et al. (2022). The panels show the results for (a) the composite debris-flow model derived in Section 2.2, (b) Meng et al.'s (2022) extended model assuming plug flow $(\alpha^g = 1.0, \quad \alpha^f = 1)$ and (c) Meng et al.'s (2022) extended model assuming shear flow $(\alpha^g = 0.6, m^g \to \infty, \quad \alpha^f = 1)$. Experimental uncertainties were not reported by Taylor-Noonan et al. (2022), so error bars are not shown.

21699011, 2026, 10, Downloaded from https://agupubs.onlinelibrary.wiley.com/doi/10.1029/2025JF008556 by The University Of Manchester, Wiley Online Library on [18/10/2026]. See the Terms and Conditions (https://onlinelibrary.wiley.com/terms-and-conditions) on Wiley Online Library for rules of use; OA articles are governed by the applicable Creative Commons License

21699011, 2026, 10, Downloaded from https://agupubs.onlinelibrary.wiley.com/doi/10.1029/2025JF008556 by The University Of Manchester, Wiley Online Library on [18/10/2026]. See the Terms and Conditions (https://onlinelibrary.wiley.com/terms-and-conditions) on Wiley Online Library for rules of use; OA articles are governed by the applicable Creative Commons License

system (3.5)–(3.11) of Meng et al. (2024), which neglects diffusion. This is because Taylor-Noonan et al.'s (2022) experiments were dominantly undersaturated during flow, so the simulations are also dominantly undersaturated, which corresponds to when Meng et al.'s (2022) original equations that are naturally in conservative form and are well-posed (Langham et al., 2025a, 2025b). Figure 10b shows that Meng et al.'s (2022) extended model assuming plug flow is able to consistently make good predictions for the tail and CoM positions as the release volume is varied. However, the model consistently over-predicts the maximum run-out distance for larger release volumes, which lies further downslope than the composite debris-flow model. One can see from the simulation in Figure 11 that the additional stretching of the front implies that the deposit is considerably thinner than Taylor-Noonan et al. (2022) measured. These results give a good indication of what could be expected with a conventional debris-flow model, provided that such a model remained well-posed (see, e.g., Bouchut et al., 2016; Iverson & George, 2014; Meng & Wang, 2016; Pelanti et al., 2008; Pitman & Le, 2005; Pudasaini, 2012). This is because they all assume plug flow through their depths, so the Darcy drag terms appear as a difference in depth-averaged species velocities just like in Equation 58.

5.4. Simulations Using Extended Meng et al. (2022) With Granular Shear

The simulation results for Meng et al.'s (2022) extended model assuming linear shear with basal slip in the grains and plug flow in the fluid, that is,

$$\alpha^g = 0.6, \quad m^g \to \infty, \quad \alpha^f = 1, \tag{63}$$

are shown in Figure 12 and Movie S12 for a release volume of 0.383 m^3/m of fluid-saturated grains per unit width. The assumed velocity shear through the flow depth is based on experimental measurements of Taylor-Noonan et al. (2022) as discussed by Meng et al. (2024) (see their Figures 5 and 14). The initial release also spreads rapidly as it flows downslope, but this time a pronounced dry front forms due to the velocity shear, and fluid is efficiently transported backwards relative to the advancing front, so no oversaturated region forms immediately behind it. In the initial stages, at least, the flow therefore remains undersaturated over its entire length.

The flow front reaches the runout plane at approximately $t = 1.39$ s, which is much earlier than the composite model and marginally faster than the plug flow model. This is a very surprising and counterintuitive result, because the velocity shear generates the largest and most resistive dry front. From a comparison of the different simulations in Movie S13, it is clear that the creation of a large dry front slightly increases the fluid depth in the undersaturated region behind the front. This in turn reduces both the basal granular friction (Equation 16) and the fluid friction in Equations 17 and 34, making the main body of grains more mobile, which then pushes the dry front slightly faster downslope than the case of the plug flow. At subsequent times, the highly resistive front plays a critical role in bringing the flow to rest in the shortest distance of all the models. As the front moves out onto the runout plane it wants to stop, but it is driven forward by the rapidly flowing undersaturated material coming off the chute. This generates a diffuse shock at the back of the front, where both the granular and fluid phases rapidly increase in thickness and decrease in velocity. The diffuse shock initially continues to propagate downstream, pushing the front forward, until approximately 3.6 s, when it stops and briefly moves slightly upslope before dissipating. The formation of a large dry front increases the frictional resistance to motion, prevents the avalanches spreading too much and brings the front to rest in almost exactly the position observed by Taylor-Noonan et al. (2022). As a result the thickness of the final deposit is much more realistic (as shown in Figure 12 at $t = 10$ s).

The preceding comparison shows that Meng et al.'s (2022) extended model with linear granular shear substantially improves the prediction of the front position relative to both the composite and plug-flow models, as shown in Figure 10c. To quantify the model performance for the front, center of mass and tail positions, the root mean square error (RMSE) is computed as

$$\mathrm{RMSE} = \sqrt{\frac{1}{N}\sum_{i=1}^{N}\left(x^i_{\mathrm{model}} - x^i_{\mathrm{exp}}\right)^2}, \tag{64}$$

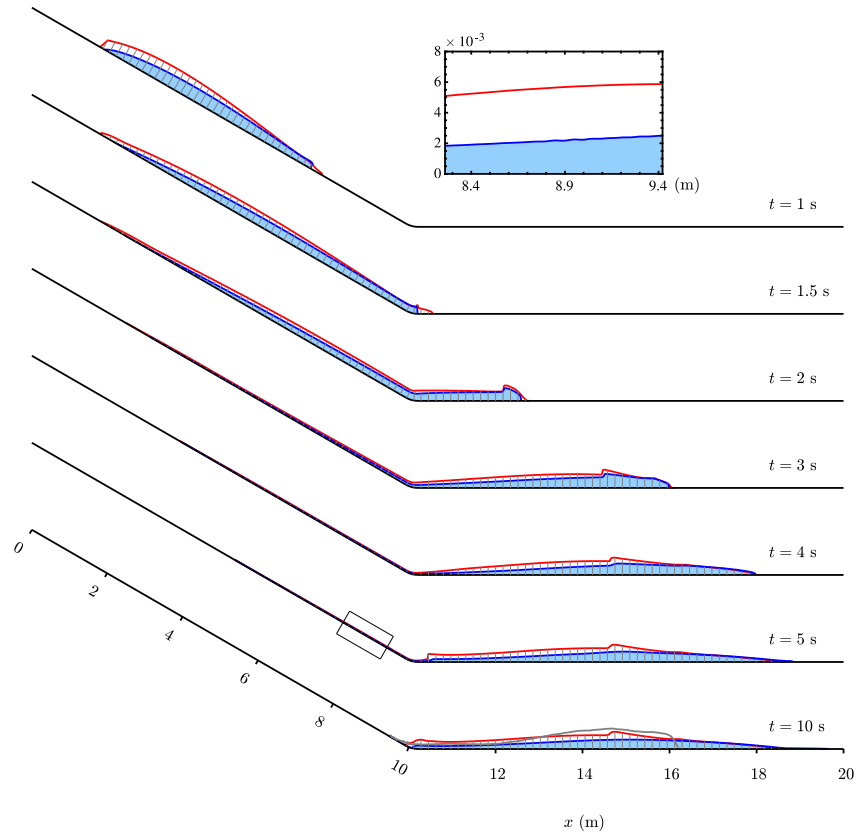


Figure 11. Computed temporal and spatial evolution of Meng et al.'s (2022) extended model assuming plug flow $(\alpha^g = 1.0, \quad \alpha^f = 1)$ after 0.383 m^3/m of fluid-saturated grains are released down Taylor-Noonan et al.'s (2022) flume. The granular free-surface is shown with a red line, the fluid free-surface with a blue line and the fluid filled region is shaded blue. Since the flow is thin, the flow thicknesses are multiplied by a factor of four and projected normally to the chute along the straight gray lines to aid visualization. The inset image shows the thin granular and fluid free-surfaces in the box indicated on the inclined section of the chute at $t = 5$ s. The gray solid line at $t = 10$ s shows the measured experimental deposit for comparison. Movie S11 shows an animation of the simulation.

where x^i_{model} and x^i_{exp} are the predicted and measured positions for each volume release $i = 1, \ldots, N$, respectively, and N is the number of release volumes. The resulting RMSE values are reported in Table 2. An arithmetic mean of the front, CoM and tail RMSE values is also reported as an aggregate measure of positional error,

$$\text{RMSE}_{\text{avg}} = \frac{1}{3}\left(\text{RMSE}_{\text{front}} + \text{RMSE}_{\text{CoM}} + \text{RMSE}_{\text{tail}}\right). \tag{65}$$

This average assigns equal weight to the three positional observables. Table 2 also shows the root integrated squared error (RISE) of the final deposit profile, which is defined as

$$\text{RISE} = \sqrt{\frac{1}{N}\sum_{i=1}^{N}\int_{x^i_{\text{tail}}}^{x^i_{\text{front}}} \left(h^g_{\text{model}} - h^g_{\text{exp}}\right)^2 \mathrm{d}x}, \tag{66}$$

where x^i_{tail} is the smaller of the predicted and measured tail positions and x^i_{front} the larger of the predicted and measured front positions for each volume release $i = 1, \ldots, N$. The resulting errors are summarized in Table 2. These metrics indicate that the shear model gives the smallest average positional RMSE and the smallest deposit-profile RISE, while also substantially improving the prediction of the front position. The plug-flow model gives the smallest RMSE values for the center of mass and tail positions individually. Experimental uncertainty estimates are not available for these data, so the comparison is based on the reported mean profiles and positions.

21699011, 2026, 10, Downloaded from https://agupubs.onlinelibrary.wiley.com/doi/10.1029/2025JF008556 by The University Of Manchester, Wiley Online Library on [18/10/2026]. See the Terms and Conditions (https://onlinelibrary.wiley.com/terms-and-conditions) on Wiley Online Library for rules of use; OA articles are governed by the applicable Creative Commons License

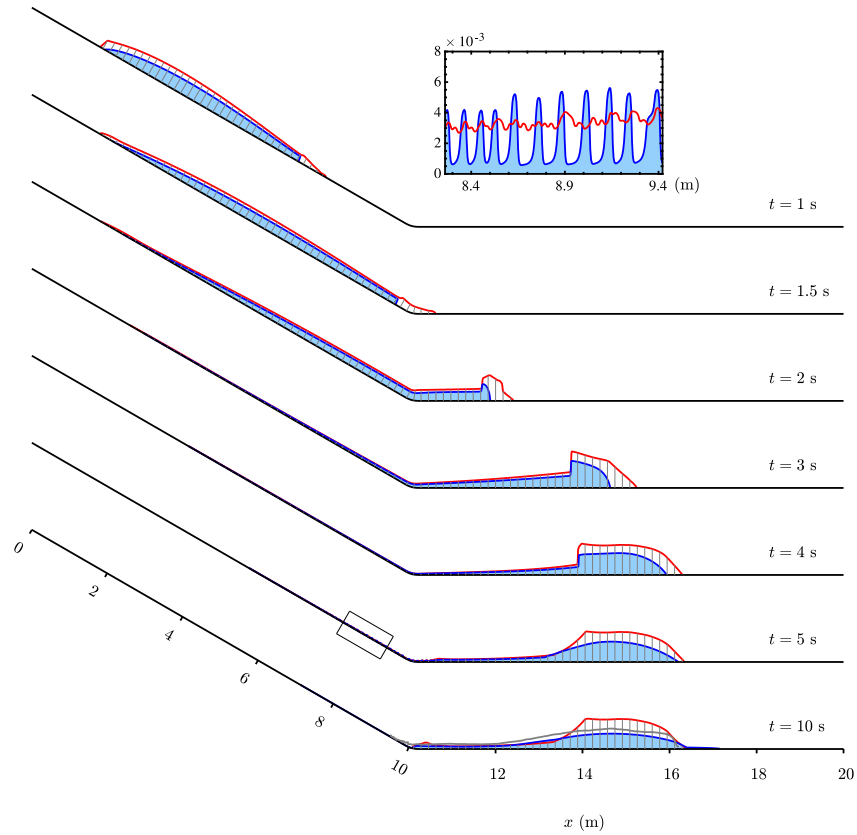


Figure 12. Computed temporal and spatial evolution of Meng et al.'s (2022) extended model assuming linear granular shear flow $\left(\alpha^g = 0.6, \quad m^g \to \infty, \quad \alpha^f = 1\right)$ after 0.383 m^3/m of fluid-saturated grains are released down Taylor-Noonan et al.'s (2022) flume. The granular free-surface is shown with a red line, the fluid free-surface with a blue line and the fluid filled region is shaded blue. Since the flow is thin, the flow thicknesses are multiplied by a factor of four and projected normally to the chute along the straight gray lines to aid visualization. The inset image shows the thin granular and fluid free-surfaces in the box indicated on the inclined section of the chute at $t = 5$ s. The gray solid line at $t = 10$ s shows the measured experimental deposit for comparison. Movie S12 shows an animation of the simulation, while Movie S13 shows a simultaneous comparison of all three models.

Since the front position controls the predicted runout extent and the deposit profile provides an integrated measure of the final deposit shape, the shear model provides the most favorable combined prediction under the metrics used here. As the most comprehensive formulation, incorporating both mobility and shear-driven species transport, it reproduces the overall runout behavior more reliably than the alternative models. The non-standard formulation of the Darcy drag therefore plays an important part in getting the overall runout correct. Since the flow in Figure 12 remains undersaturated throughout almost its entire evolution, it is unsurprising that the results look almost identical to those in Figure 9 of Meng et al. (2024). The main differences are in the type of waves that form in the thin tails (as shown in the inset boxes). Note that the computed flow dynamics and deposit morphology

Table 2
Comparison of the Root Mean Square Error (RMSE) for the Front, Center of Mass (CoM), Tail and Average Positions, as Well as the Root Integrated Squared (RISE) of the Deposit Profile for the Three Models

Model	Front RMSE (m)	CoM RMSE (m)	Tail RMSE (m)	Average RMSE (m)	Deposit RISE ($m^{3/2}$)
Composite model	1.640	1.086	0.126	0.951	0.0777
Meng's plug	1.970	0.273	0.123	0.789	0.0641
Meng's shear	0.345	0.548	0.199	0.364	0.0615

Note. The average RMSE is the arithmetic mean of the front, CoM, and tail RMSE values and is used as an aggregate measure of positional error; the deposit-profile RISE is reported separately because it has different dimensions.

21699011, 2026, 10, Downloaded from https://agupubs.onlinelibrary.wiley.com/doi/10.1029/2025JF008556 by The University Of Manchester, Wiley Online Library on [18/10/2026]. See the Terms and Conditions (https://onlinelibrary.wiley.com/terms-and-conditions) on Wiley Online Library for rules of use; OA articles are governed by the applicable Creative Commons License

21699011, 2026, 10, Downloaded from https://agupubs.onlinelibrary.wiley.com/doi/10.1029/2025JF008556 by The University Of Manchester, Wiley Online Library on [18/10/2026]. See the Terms and Conditions (https://onlinelibrary.wiley.com/terms-and-conditions) on Wiley Online Library for rules of use; OA articles are governed by the applicable Creative Commons License

are not particularly sensitive to the specific choice of the velocity profile, provided that the overall shear magnitude remains comparable, consistent with Meng et al. (2024).

6. Discussion and Conclusions

In this paper, the multiphase debris-flow model of Meng et al. (2022) is extended by adding a depth-averaged granular viscous term (Equation 13) to the granular momentum balance (Equation 9). The resulting system of equations therefore has physically motivated depth-averaged viscous-like terms in both the granular and the fluid momentum balances (Gray & Edwards, 2014). This ensures that the theory is unconditionally well-posed (Langham et al., 2025a, 2025b), which means that small perturbations do not grow at an unbounded rate in the high wave number (short wavelength) limit. Langham et al. (2025a, 2025b) showed that conventional hyperbolic/mixed-type multiphase debris-flow models do not have this structure, and consequently most have regions of parameter space where the equations are ill-posed (see, e.g., Bouchut et al., 2016; Iverson & George, 2014; Meng & Wang, 2016; Pelanti et al., 2008; Pitman & Le, 2005; Pudasaini, 2012). Ill-posedness is a common problem when developing new mathematical models, and should not be ignored. This is because a formal mathematical solution does not exist in the ill-posed regions, and consequently numerical solutions of the equations do not converge to a solution on grid-resolution refinement, although they may predict plausible looking results at a given resolution due to numerical diffusion.

A numerical method is formulated and implemented in Section 3 to solve Meng et al.'s (2022) extended system of equations which include non-conservative and diffusive terms (see Equations 13 and 14). Non-conservative terms can be problematic in hyperbolic systems, especially when discontinuous inviscid shocks develop, as it is then unclear how to formulate jump conditions across them (Chadwick, 1976). An added benefit of adding the extra depth-averaged granular viscous term in Equation 13 is that discontinuous inviscid shocks are regularized into smooth, finite-width transition layers. Thus, the non-conservative terms are less difficult to handle in the present viscously regularized system.

In Section 4 the numerical method is used to compute the infiltration of a fluid into a static pile of grains. The results in Figures 2 and 3 and Movies S1 and S2, show that for a linear shear profile in the grains and plug flow in the fluid, the flow naturally develops into a traveling wave with a large amplitude dry front that is pushed downslope by an increasingly fluid-rich tail. Meng et al. (2022) showed that these types of solution are able to quantitatively explain the small-scale traveling waves observed in Davies's (1990) moving-bed flume experiments. More importantly, large amplitude debris-flow surges frequently develop in steep mountainous terrain and move at very high speeds, see, for example, Movie 1 of Meng et al. (2022). Most conventional debris flow models neglect velocity shear, and as a result the fronts spread out (see Figures 7 and 8; Movies S8 and S9). Such models are therefore missing an important mechanism for concentrating the destructive potential of debris-flows in a large amplitude surge.

The fluid infiltration problem also provides a perfect example to illustrate how ill-posedness occurs in inviscid calculations, when the depth-averaged viscous terms in Equations 13 and 14 are neglected. Figure 4 and Movie S4 show that as the fluid first infiltrates into the grains, a series of short-wavelength oscillations rapidly grow and contaminate the solution in the oversaturated region. This is the region of parameter space where ill-posedness is expected (Langham et al., 2025a, 2025b). However, in order to show ill-posedness numerically, it is necessary to perform a grid refinement study. Figures 5a–5c and Movies S3–S5 show the same solution at a range of grid resolutions. At relatively low grid resolution (Figure 5a), there is no sign of the oscillations, but as the numerical grid is progressively refined, the oscillations become finer scaled and grow faster. This behavior is typical of ill-posed problems and results from the fact that the numerical method is inherently diffusive, with a diffusion coefficient that is dependent on the grid resolution. In Figure 5a, the diffusion is high enough to suppress obvious signs of ill-posedness, but as the numerical diffusion is reduced the oscillations appear and become more pronounced. In the limit of infinite grid resolution, there would be no numerical diffusion and the instability would grow at an infinite rate and the numerical method would fail. Formally, if regions of parameter space become ill-posed, then there is no mathematical solution of the problem. Conversely, when Meng et al.'s (2022) extended model (with viscous terms) is solved over the same range of grid resolutions the solutions converge to a unique solution, as shown in Figure 5d and Movies S1, S6, and S7. It is important to stress that this is not just a numerical regularization of the problem. The form of the viscous terms in Equations 13 and 14 is derived from granular and fluid constitutive laws that bring essential new physics into the problem (GDR-MiDi, 2004; Gray &

21699011, 2026, 10, Downloaded from https://agupubs.onlinelibrary.wiley.com/doi/10.1029/2025JF008556 by The University Of Manchester, Wiley Online Library on [18/10/2026]. See the Terms and Conditions (https://onlinelibrary.wiley.com/terms-and-conditions) on Wiley Online Library for rules of use; OA articles are governed by the applicable Creative Commons License

Edwards, 2014; Jop et al., 2006). Using an unconditionally well-posed model, such as the extended model of Meng et al. (2022) derived here, has the big advantage that the integrity of the solution is guaranteed over the whole of parameter space.

Meng et al.'s (2022) debris-flow theory departs from conventional plug-flow debris-flow models by incorporating the vertical structure of the grain-fluid mixture and the resulting internal shear through the flow depth. It consists of two depth-averaged mass balances and two depth-averaged momentum balances for the grain and fluid heights and velocities, respectively. Different regions of the flow can simultaneously be (a) dry, (b) undersaturated, and (c) oversaturated or pure fluid phases. The really important idea in Meng et al.'s (2022) model is the way that the interspecies Darcy drag is handled in the source terms (Equations 16 and 17). Rather than just assuming plug flow through the depth (which leads to depth-averaged velocity differences in Equation 58), Meng et al.'s (2022) model computes the relative motion of the two species in the lower saturated flow, where both the grain and the fluid coexist. This leads to a non-standard Darcy drag, such as that given in Equation 47. This structure facilitates two mechanisms for the relative transport of grains and fluid. First, there is standard mobility-driven transport that arises through the difference in depth-averaged species velocities (see Bouchut et al., 2016; Pelanti et al., 2008; Pitman & Le, 2005; Pudasaini, 2012). Second, there is the combination of vertical structure and velocity shear, which until recently had been completely missed, despite its well-documented importance in size-disperse granular flows (see Baker, Johnson, & Gray, 2016; Gray, 2018; Gray & Kokelaar, 2010) and particle-laden suspensions (see Acrivos et al., 1992).

In Section 5, the numerical method is used to compute how three variants of Meng et al.'s (2022) extended model flow down an inclined plane and out over a horizontal runout pad. The first is a composite debris-flow model (derived in Section 2.2), the second corresponds to a plug flow assumption for both species and the third assumes linear shear and basal slip in the grains. This hierarchy of models starts with no vertical structure or relative motion and progressively adds mobility-driven relative transport and velocity shear, while ensuring that the applied friction laws and diffusivities are unchanged. The results are shown in Figures 9, 11, and 12 and Movies S10–S13.

Movie S13 is particularly useful because it simultaneously shows an animation of all three cases. Surprisingly, the saturated composite debris-flow model has minimal granular friction, but moves the slowest down the inclined plane, because of the quadratic velocity dependent fluid drag which penalizes rapid motion. It also has the longest overall runout of its CoM, as shown in Figure 10a. The two multiphase simulations both move much faster down the inclined chute, because the granular momentum balance is only indirectly affected by the quadratic velocity-dependent fluid drag via the Darcy drag coupling. Bizarrely, the model with velocity shear generates a large resistive dry front, but its flow front is the first to reach the runout plane. Once on the run-out plane, this dry resistive front is responsible for stopping the front in the shortest distance at almost exactly the position measured in Taylor-Noonan et al.'s (2022) large-scale flume experiments. The tail and CoM positions are also in excellent quantitative agreement (see Figure 10c). The best overall CoM position is achieved by the multiphase plug flow model, but this good agreement comes at the expense of dramatically over-predicting the maximum runout distance (Figure 10b). These contrasts imply that the appropriate level of model complexity is governed by the dominant mechanisms active within the flow. Where interest lies primarily in bulk motion and overall runout dynamics, simplified formulations may provide satisfactory predictions. However, when dry fronts form and control runout, or when strong velocity gradients are expected within the flow, models that explicitly resolve velocity shear and vertical structure are required to obtain physically reliable results. In conclusion, phase-separation phenomena can generate some unexpected and counterintuitive feedback effects that are very important for the dynamics of debris flows.

While the present formulation captures shear-induced phase separation, it does not yet account for particle-size segregation or polydispersity effects. A logical next step would be to combine two-phase debris-flow models with multiphase depth-averaged models for particle-size segregation. This would, for instance, allow large amplitude drier bouldery fronts to be modeled, which are frequently observed in debris flows (Iverson, 1997; Meng et al., 2022; Pierson, 1986). Much of the theoretical groundwork for this has now been done (Baker, Barker, & Gray, 2016; Baker, Johnson, & Gray, 2016; Edwards et al., 2023; Gray & Edwards, 2014; Gray & Kokelaar, 2010; Langham et al., 2025a, 2025b; Meng et al., 2022, 2024). However, without this work one would not be aware of the resonances that occur between the equations, which lead to unbounded short-wavelength instabilities and mathematical ill-posedness. Nor would one have understood how to circumvent these problems by including

more details of the rheology in these models. As one moves to more complex systems with three or more species, the number of equations will increase and there will be more potential for ill-posedness, especially if these important lessons are not heeded. In particular, if the resulting systems do not have a diagonal diffusion operator, with strictly positive diffusion coefficients in each momentum equation and zeros in each mass balance, then one should be suspicious about the integrity of numerical computations and carefully test to see whether they are grid-resolution converged or not (Langham et al., 2025a, 2025b).

Appendix A: Fluxes and Source Terms

In the undersaturated regime, $(1-\phi^c)H^g > \phi^c H^f$, the convective flux vector

$$\boldsymbol{F}(\boldsymbol{U}) = \begin{pmatrix} M^g \\ \dfrac{(M^g)^2}{H^g} + \dfrac{1}{2}\dfrac{(H^g)^2}{\phi^c} g\cos\zeta - \dfrac{1}{2}\gamma\phi^c\left(\dfrac{H^f}{1-\phi^c}\right)^2 g\cos\zeta \\ M^f \\ \dfrac{(M^f)^2}{H^f} + \dfrac{1}{2}\left(\dfrac{H^f}{1-\phi^c}\right)^2 g\cos\zeta \end{pmatrix}, \tag{A1}$$

and the non-conservative product vector

$$\boldsymbol{N}(\boldsymbol{U},\boldsymbol{U}_x) = \begin{pmatrix} 0 \\ -\gamma\phi^c \dfrac{H^f}{(1-\phi^c)^2} g\cos\zeta \dfrac{\partial H^f}{\partial x} \\ 0 \\ \phi^c \dfrac{H^f}{(1-\phi^c)^2} g\cos\zeta \dfrac{\partial H^f}{\partial x} \end{pmatrix}. \tag{A2}$$

In the over-saturated regime, $(1-\phi^c)H^g \leq \phi^c H^f$, the flux vector

$$\boldsymbol{F}(\boldsymbol{U}) = \begin{pmatrix} M^g \\ \dfrac{(M^g)^2}{H^g} + \dfrac{1}{2}\dfrac{(H^g)^2}{\phi^c} g\cos\zeta - \dfrac{1}{2}\gamma\dfrac{(H^g)^2}{\phi^c} g\cos\zeta \\ M^f \\ \dfrac{(M^f)^2}{H^f} + \dfrac{1}{2}\left(H^f + H^g\right)^2 g\cos\zeta \end{pmatrix}, \tag{A3}$$

and the non-conservative product vector

$$\boldsymbol{N}(\boldsymbol{U},\boldsymbol{U}_x) = \begin{pmatrix} 0 \\ -\gamma(g\cos\zeta)H^g\left(\dfrac{\partial H^f}{\partial x} + \dfrac{\partial H^g}{\partial x}\right) \\ 0 \\ (g\cos\zeta)H^g\left(\dfrac{\partial H^f}{\partial x} + \dfrac{\partial H^g}{\partial x}\right) \end{pmatrix}. \tag{A4}$$

The diffusive flux vector $\boldsymbol{D}$ is defined as

21699011, 2026, 10, Downloaded from https://agupubs.onlinelibrary.wiley.com/doi/10.1029/2025JF008556 by The University Of Manchester, Wiley Online Library on [18/10/2026]. See the Terms and Conditions (https://onlinelibrary.wiley.com/terms-and-conditions) on Wiley Online Library for rules of use; OA articles are governed by the applicable Creative Commons License

$$\boldsymbol{D}(\boldsymbol{U},\boldsymbol{U}_x)=\begin{pmatrix}0\\ 2\nu^g\left(\dfrac{\partial M^g}{\partial x}-\dfrac{M^g}{H^g}\dfrac{\partial H^g}{\partial x}\right)\\ 0\\ 2\nu^f\left(\dfrac{\partial M^f}{\partial x}-\dfrac{M^f}{H^f}\dfrac{\partial H^f}{\partial x}\right)\end{pmatrix}. \tag{A5}$$

where the depth-averaged granular viscosity

$$\nu^g=\frac{1}{2}\hat{\nu}^g\left(\frac{H^g}{\phi^c}\right)^{\frac{1}{2}}. \tag{A6}$$

The source vector $\boldsymbol{S}$ is defined as

$$\boldsymbol{S}(\boldsymbol{U})=\begin{pmatrix}0, & \mathcal{L}^g, & 0, & \mathcal{L}^f\end{pmatrix}^{\mathrm{T}}. \tag{A7}$$

Appendix B: Characteristic Wave Speeds

The characteristic wave speeds entering the numerical flux are, in principle, influenced by both the conservative advective terms and the non-conservative coupling terms. Retaining the non-conservative terms in the characteristic analysis leads to a quartic characteristic polynomial, for which a compact analytical representation of the full eigenstructure is not available in a form suitable for a practical characteristic wave-speed estimate. The wave-speed estimate adopted here is therefore constructed from the conservative advective part of the system.

The omitted non-conservative contribution is associated primarily with the buoyancy-related coupling. For the regimes considered in the present simulations, the non-dimensional form of the solid momentum equation indicates that this contribution is small, compared to the leading-order inertial or advective terms, consistent with the order-of-magnitude scaling of the buoyancy-related terms in the nondimensional solid momentum balance of Pitman and Le (2005). Its effect on the local propagation speeds is therefore treated as a higher-order correction to the advective wave speeds used in the CFL condition. This approximation is a limitation of the present implementation, but it is appropriate for the parameter range considered here.

The role of the characteristic wave speed in the present scheme is to set the amount of numerical viscosity in the convective flux. Since the governing Equations 8–11 include finite physical viscosity in the grain and water momentum equations, the numerical viscosity associated with the flux decreases under mesh refinement, whereas the physical viscosity remains fixed. Consequently, in the grid-converged limit, the computed solutions are governed by the finite-viscosity regularized system rather than by the numerical dissipation associated with the neglected component of the wave-speed estimate.

Based on these considerations, the Jacobian matrix is approximated by $\boldsymbol{A}=\partial\boldsymbol{F}/\partial\boldsymbol{U}$, whose eigenvalues represent characteristic wave speeds. In the undersaturated regime, the numerical flux is given by Equation A1, and hence the corresponding Jacobian matrix is

$$\boldsymbol{A}=\begin{pmatrix}0 & 1 & 0 & 0\\ -\dfrac{(M^g)^2}{(H^g)^2}+\dfrac{H^g}{\phi^c}g\cos\zeta & \dfrac{2M^g}{H^g} & -\dfrac{\gamma\phi^c}{(1-\phi^c)^2}H^f g\cos\zeta & 0\\ 0 & 0 & 0 & 1\\ 0 & 0 & -\dfrac{(M^f)^2}{(H^f)^2}+\dfrac{H^f}{(1-\phi^c)^2}g\cos\zeta & \dfrac{2M^f}{H^f}\end{pmatrix}. \tag{B1}$$

21699011, 2026, 10, Downloaded from https://agupubs.onlinelibrary.wiley.com/doi/10.1029/2025JF008556 by The University Of Manchester, Wiley Online Library on [18/10/2026]. See the Terms and Conditions (https://onlinelibrary.wiley.com/terms-and-conditions) on Wiley Online Library for rules of use; OA articles are governed by the applicable Creative Commons License

The characteristic wave speeds are given by solving for the eigenvalues λ using $|\boldsymbol{A} - \lambda\mathbf{1}| = 0$, where $\mathbf{1}$ is the identity matrix. In conservative variables the characteristics are

$$\lambda_{1,2} = \frac{M^g}{H^g} \pm \sqrt{\frac{H^g g \cos\zeta}{\phi^c}}, \qquad \lambda_{3,4} = \frac{M^f}{H^f} \pm \frac{\sqrt{H^f g \cos\zeta}}{1-\phi^c}. \tag{B2a, b}$$

In field variables the characteristics are

$$\lambda_{1,2} = \bar{u}^g \pm \sqrt{h^g g \cos\zeta}, \qquad \lambda_{3,4} = \bar{u}^f \pm \sqrt{\frac{h^f g \cos\zeta}{1-\phi^c}}. \tag{B3a, b}$$

In the oversaturated regime, the numerical flux is defined in Equation A3 and the corresponding Jacobian matrix is

$$\boldsymbol{A} = \begin{pmatrix} 0 & 1 & 0 & 0 \\ -\dfrac{(M^g)^2}{(H^g)^2} + \dfrac{H^g}{\phi^c} g\cos\zeta - \dfrac{\gamma H^g}{\phi^c} g\cos\zeta & \dfrac{2M^g}{H^g} & 0 & 0 \\ 0 & 0 & 0 & 1 \\ \left(H^f + H^g\right) g\cos\zeta & 0 & -\dfrac{\left(M^f\right)^2}{\left(H^f\right)^2} + \left(H^f + H^g\right) g\cos\zeta & \dfrac{2M^f}{H^f} \end{pmatrix}. \tag{B4}$$

Solving characteristic polynomial gives rise to four eigenvalues, and they are given by

$$\lambda_{1,2} = \frac{M^g}{H^g} \pm \sqrt{\frac{(1-\gamma)H^g g\cos\zeta}{\phi^c}}, \qquad \lambda_{3,4} = \frac{M^f}{H^f} \pm \sqrt{H^f g\cos\zeta + H^g g\cos\zeta} \tag{B5a, b}$$

in conservative variables. In field variables, the characteristics are

$$\lambda_{1,2} = \bar{u}^g \pm \sqrt{(1-\gamma)h^g g\cos\zeta}, \qquad \lambda_{3,4} = \bar{u}^f \pm \sqrt{h^f g\cos\zeta}. \tag{B6a, b}$$

Note that the wave speeds in both the undersaturated and oversaturated regimes are real, and hence can be used to compute the numerical fluxes $\boldsymbol{H}_{j+\frac{1}{2}}(t)$ and $\boldsymbol{H}_{j-\frac{1}{2}}(t)$.

Conflict of Interest

The authors declare no conflicts of interest relevant to this study.

Availability Statement

The computer codes and simulation data are available in the Harvard Dataverse (Meng et al., 2025; https://doi.org/10.7910/DVN/OUWQLV).

Acknowledgments
This research was supported by the National Natural Science Foundation of China (NSFC) under grant Nos. 12272074 and 12672531, the Liaoning Revitalization Talents Program (Grant No. XLYC2203149), and the Fundamental Research Funds (Grant No. 3132026180) for the Central Universities. C. G. Johnson and J. M. N. T. Gray gratefully acknowledge support from the UK Natural Environment Research Council (NERC) through grant Nos. NE/X00029X/1 and NE/X013936/1. Additionally, this research partially benefited from the European Commission's Marie Skłodowska-Curie Individual Fellowships (IF) programme under grant No. 792967. J. M. N. T. Gray was also supported by a Royal Society Wolfson Research Merit Award (WM150058) and an EPSRC Established Career Fellowship (EP/M022447/1).

References

Aaron, J., Langham, J., Spielmann, R., Hirschberg, J., McArdell, B., Boss, S., et al. (2025). Detailed observations reveal the genesis and dynamics of destructive debris-flow surges. *Communications Earth & Environment*, *6*(1), 556. https://doi.org/10.1038/s43247-025-02488-7

Acrivos, A., Batchelor, G. K., Hinch, E. J., Koch, D. L., & Mauri, R. (1992). Longitudinal shear-induced diffusion of spheres in a dilute suspension. *Journal of Fluid Mechanics*, *240*(1), 651–657.

Baker, J., Barker, T., & Gray, J. M. N. T. (2016). A two-dimensional depth-averaged μ(I)-rheology for dense granular avalanches. *Journal of Fluid Mechanics*, *787*, 367–395. https://doi.org/10.1017/jfm.2015.684

Baker, J., Johnson, C. G., & Gray, J. M. N. T. (2016). Segregation-induced finger formation in granular free-surface flows. *Journal of Fluid Mechanics*, *809*, 168–212. https://doi.org/10.1017/jfm.2016.673

Barker, T., Rauter, M., Maguire, E. S. F., Johnson, C. G., & Gray, J. M. N. T. (2021). Coupling rheology and segregation in granular flows. *Journal of Fluid Mechanics*, *909*, A22. https://doi.org/10.1017/jfm.2020.973

21699011, 2026, 10, Downloaded from https://agupubs.onlinelibrary.wiley.com/doi/10.1029/2025JF008556 by The University Of Manchester, Wiley Online Library on [18/10/2026]. See the Terms and Conditions (https://onlinelibrary.wiley.com/terms-and-conditions) on Wiley Online Library for rules of use; OA articles are governed by the applicable Creative Commons License

Berger, M. J., & LeVeque, R. J. (1998). Adaptive mesh refinement using wave-propagation algorithms for hyperbolic systems. *SIAM Journal on Numerical Analysis*, *35*(6), 2298–2316. https://doi.org/10.1137/s0036142997315974

Bouchut, F., Fernández-Nieto, E. D., Mangeney, A., & Narbona-Reina, G. (2016). A two-phase two-layer model for fluidized granular flows with dilatancy effects. *Journal of Fluid Mechanics*, *801*, 166–221. https://doi.org/10.1017/jfm.2016.417

Boyer, F., Guazzelli, É., & Pouliquen, O. (2011). Unifying suspension and granular rheology. *Physical Review Letters*, *107*(18), 188301. https://doi.org/10.1103/physrevlett.107.188301

Carman, P. (1937). Fluid flow through granular beds. *Transactions of the Institution of Chemical Engineers*, *15*, 150–166.

Cauret, J. J., Colombeau, J. F., & Le Roux, A. Y. (1989). Discontinuous generalized solutions of nonlinear nonconservative hyperbolic equations. *Journal of Mathematical Analysis and Applications*, *139*, 552–573.

Chadwick, P. (1976). *Continuum mechanics. Concise theory and problems*. George Allen & Unwin.

Chertock, A., Cui, S., Kurganov, A., & Wu, T. (2015). Well-balanced positivity preserving central-upwind scheme for the shallow water system with friction terms. *International Journal for Numerical Methods in Fluids*, *78*(6), 355–383. https://doi.org/10.1002/fld.4023

Davies, T. R. H. (1990). Debris flow surges-experimental simulation. *Journal of Hydrology (New Zealand)*, *29*(1), 18–46.

Denissen, I. F. C., Weinhart, T., Voortwis, A. T., Luding, S., Gray, J. M. N. T., & Thornton, A. R. (2019). Bulbous head formation in bidisperse shallow granular flow over an inclined plane. *Journal of Fluid Mechanics*, *866*, 263–297.

Edwards, A. N., Rocha, F., Kokelaar, B. P., Johnson, C. G., & Gray, J. M. N. T. (2023). Particle-size segregation in self-channelised granular flows. *Journal of Fluid Mechanics*, *955*, A38.

GDR-MiDi. (2004). On dense granular flows. *European Physical Journal E*, *14*(4), 341–365. https://doi.org/10.1140/epje/i2003-10153-0

Goharzadeh, A., Khalili, A., & Jørgensen, B. B. (2005). Transition layer thickness at a fluid-porous interface. *Physics of Fluids*, *17*(5), 057102. https://doi.org/10.1063/1.1894796

Gray, J. M. N. T. (2018). Particle segregation in dense granular flows. *Annual Review of Fluid Mechanics*, *50*(1), 407–433. https://doi.org/10.1146/annurev-fluid-122316-045201

Gray, J. M. N. T., & Ancey, C. (2009). Segregation, recirculation and deposition of coarse particles near two-dimensional avalanche fronts. *Journal of Fluid Mechanics*, *629*, 387–423. https://doi.org/10.1017/s0022112009006466

Gray, J. M. N. T., & Edwards, A. N. (2014). A depth-averaged μ(I)-rheology for shallow granular free-surface flows. *Journal of Fluid Mechanics*, *755*, 503–534. https://doi.org/10.1017/jfm.2014.450

Gray, J. M. N. T., & Kokelaar, B. P. (2010). Large particle segregation, transport and accumulation in granular free-surface flows. *Journal of Fluid Mechanics*, *652*, 105–137. https://doi.org/10.1017/s002211201000011x

Guazzelli, É., & Pouliquen, O. (2018). Rheology of dense granular suspensions. *Journal of Fluid Mechanics*, *852*, P1. https://doi.org/10.1017/jfm.2018.548

Iverson, R. M. (1997). The physics of debris flows. *Reviews of Geophysics*, *35*(3), 245–296. https://doi.org/10.1029/97rg00426

Iverson, R. M. (2003). The debris-flow rheology myth. In D. Rickenmann, & C. L. Chen (Ed.), *Debris-flow hazards mitigation: Mechanics, prediction, and assessment* (pp. 303–314). Millpress.

Iverson, R. M., & Denlinger, R. P. (2001). Flow of variably fluidized granular masses across three-dimensional terrain: 1. Coulomb mixture theory. *Journal of Geophysical Research*, *106*(B1), 537–552. https://doi.org/10.1029/2000jb900329

Iverson, R. M., & George, D. L. (2014). A depth-averaged debris-flow model that includes the effects of evolving dilatancy. I. Physical basis. *Proceedings of the Royal Society of London A*, *470*(2170), 20130819. https://doi.org/10.1098/rspa.2013.0819

Johnson, C. G., Kokelaar, B. P., Iverson, R. M., Logan, M., Lahusen, R. G., & Gray, J. M. N. T. (2012). Grain-size segregation and levee formation in geophysical mass flows. *Journal of Geophysical Research: Earth Surface*, *117*(F1), F01032. https://doi.org/10.1029/2011jf002185

Jop, P., Forterre, Y., & Pouliquen, O. (2006). A constitutive law for dense granular flows. *Nature*, *441*(7094), 727–730. https://doi.org/10.1038/nature04801

Joseph, D. D., & Saut, J. C. (1990). Short-wave instabilities and ill-posed initial-value problems. *Theoretical and Computational Fluid Dynamics*, *1*(4), 191–227. https://doi.org/10.1007/bf00418002

Kean, J. W., McCoy, S. W., Tucker, G. E., Staley, D. M., & Coe, J. A. (2013). Runoff-generated debris flows: Observations and modeling of surge initiation, magnitude, and frequency. *Journal of Geophysical Research: Earth Surface*, *118*(4), 2190–2207. https://doi.org/10.1002/jgrf.20148

Kurganov, A., & Petrova, G. (2009). Central-upwind schemes for two-layer shallow equations. *SIAM Journal on Scientific Computing*, *31*(3), 1742–1773. https://doi.org/10.1137/080719091

Kurganov, A., & Tadmor, E. (2000). New high-resolution central schemes for nonlinear conservation laws and convection–diffusion equations. *Journal of Computational Physics*, *160*(1), 241–282. https://doi.org/10.1006/jcph.2000.6459

Langham, J., Meng, X., Webb, J. P., Johnson, C. G., & Gray, J. M. N. T. (2025a). Ill posedness in shallow multi-phase debris flow models. *Journal of Fluid Mechanics*, *1015*, A52. https://doi.org/10.1017/jfm.2025.10297

Langham, J., Meng, X., Webb, J. P., Johnson, C. G., & Gray, J. M. N. T. (2025b). Ill posedness in shallow multi-phase debris flow models – Corrigendum. *Journal of Fluid Mechanics*, *1022*, E2. https://doi.org/10.1017/jfm.2025.10762

Lukashov, S. G., Lancaster, J. T., & Oakley, N. S. (2019). Post-fire debris flows of 9 January 2018, Thomas Fire, Southern California: Initiation areas, precipitation and impacts. In *Debris-flow hazards mitigation: Mechanics, monitoring, modeling, and assessment. Proceedings of the Seventh International Conference on Debris-Flow Hazards Mitigation, Golden, Colorado, USA* (pp. 774–781).

Manning, R. (1891). On the flow of water in open channel and pipes. *Transactions, Institution of Civil Engineers of Ireland*, *20*, 161–207.

Meng, X., Johnson, C., & Gray, J. M. N. T. (2022). Formation of dry granular fronts and watery tails in debris flows. *Journal of Fluid Mechanics*, *943*, A19. https://doi.org/10.1017/jfm.2022.400

Meng, X., Taylor-Noonan, A. M., Johnson, C. G., Take, W. A., Bowman, E. T., & Gray, J. M. N. T. (2024). Granular-fluid avalanches: The role of vertical structure and velocity shear. *Journal of Fluid Mechanics*, *980*, A11. https://doi.org/10.1017/jfm.2023.1023

Meng, X., & Wang, Y. (2016). Modelling and numerical simulation of two-phase debris flows. *Acta Geotechnica*, *11*(5), 1027–1045. https://doi.org/10.1007/s11440-015-0418-4

Meng, X., & Wang, Y. (2018). Modeling dynamic flows of grain–fluid mixtures by coupling the mixture theory with a dilatancy law. *Acta Mechanica*, *229*(6), 2521–2538. https://doi.org/10.1007/s00707-018-2111-9

Meng, X., Wang, Y., Wang, C., & Fischer, J. (2017). Modeling of unsaturated granular flows by a two-layer approach. *Acta Geotechnica*, *12*(3), 677–701. https://doi.org/10.1007/s11440-016-0509-x

Meng, X., Zhao, L., Johnson, C. G., & Gray, J. M. N. T. (2025). Well-posed debris-flow models with phase separation [dataset]. *Harvard Dataverse*. https://doi.org/10.7910/DVN/OUWQLV

Ovsyannikov, L. V. (1979). Two-layer "shallow water" model. *Journal of Applied Mechanics and Technical Physics*, *20*(2), 127–135. https://doi.org/10.1007/bf00910010

21699011, 2026, 10, Downloaded from https://agupubs.onlinelibrary.wiley.com/doi/10.1029/2025JF008556 by The University Of Manchester, Wiley Online Library on [18/10/2026]. See the Terms and Conditions (https://onlinelibrary.wiley.com/terms-and-conditions) on Wiley Online Library for rules of use; OA articles are governed by the applicable Creative Commons License

Patra, A., Bauer, C., Nichita, C., Pitman, E., Sheridan, M., Bursik, M., et al. (2005). Parallel adaptive numerical simulation of dry avalanches over natural terrain. *Journal of Volcanology and Geothermal Research*, *139*(1–2), 1–21. https://doi.org/10.1016/j.jvolgeores.2004.06.014

Pelanti, M., Bouchut, F., & Mangeney, A. (2008). A Roe-type scheme for two-phase shallow granular flows over variable topography. *ESAIM: Mathematical Modelling and Numerical Analysis*, *42*(5), 851–885. https://doi.org/10.1051/m2an:2008029

Pierson, T. C. (1986). Flow behavior of channelized debris flows, Mount St. Helens. In A. Abrahams (Ed.), *Hillslope processes* (pp. 269–296). Allen and Unwin.

Pitman, E. B., & Le, L. (2005). A two-fluid model for avalanche and debris flows. *Philosophical Transactions of the Royal Society A*, *363*(1832), 1573–1601. https://doi.org/10.1098/rsta.2005.1596

Pouliquen, O., Delour, J., & Savage, S. B. (1997). Fingering in granular flows. *Nature*, *386*(6627), 816–817. https://doi.org/10.1038/386816a0

Pouliquen, O., & Forterre, Y. (2002). Friction law for dense granular flows: Application to the motion of a mass down a rough inclined plane. *Journal of Fluid Mechanics*, *453*, 133–151. https://doi.org/10.1017/s0022112001006796

Pudasaini, S. P. (2012). A general two-phase debris flow model. *Journal of Geophysical Research: Earth Surface*, *117*(F3), F03010. https://doi.org/10.1029/2011jf002186

Pudasaini, S. P., & Mergili, M. (2019). A multi-phase mass flow model. *Journal of Geophysical Research: Earth Surface*, *124*(12), 2920–2942. https://doi.org/10.1029/2019jf005204

Saingier, G., Deboeuf, S., & Lagrée, P. -Y. (2016). On the front shape of an inertial granular flow down a rough incline. *Physics of Fluids*, *28*(5), 053302. https://doi.org/10.1063/1.4948401

Savage, S. B., & Hutter, K. (1989). The motion of a finite mass of granular material down a rough incline. *Journal of Fluid Mechanics*, *199*, 177–215. https://doi.org/10.1017/s0022112089000340

Savage, S. B., & Hutter, K. (1991). The dynamics of avalanches of granular materials from initiation to run-out. I. Analysis. *Acta Mechanica*, *86*(1–4), 201–223. https://doi.org/10.1007/bf01175958

Shugar, D. E. A., Jacquemart, M., Shean, D., Bhushan, S., Upadhyay, K., Sattar, A., et al. (2021). A massive rock and ice avalanche caused the 2021 disaster at Chamoli, Indian Himalaya. *Science*, *373*(6552), 300–306. https://doi.org/10.1126/science.abh4455

Sun, W., Meng, X., Wang, Y., Hsiau, S., & You, Z. (2023). A depth-averaged description of submarine avalanche flows and induced surface waves. *Journal of Geophysical Research: Earth Surface*, *128*(4), e2022JF006893. https://doi.org/10.1029/2022jf006893

Sun, W., & Wang, Y. (2024). Modeling phase separation in grain-fluid mixture flows by a depth-averaged approach with dilatancy effects. *Journal of Geophysical Research: Earth Surface*, *129*(12), e2023JF007416. https://doi.org/10.1029/2023jf007416

Taylor-Noonan, A. M., Bowman, E. T., McArdell, B., Kaitna, R., McElwaine, J. N., & Take, W. A. (2022). Influence of pore fluid on grain-scale interactions and mobility of granular flows of differing volume. *Journal of Geophysical Research: Earth Surface*, *127*(12), e2022JF006622. https://doi.org/10.1029/2022jf006622

Viroulet, S., Baker, J. L., Edwards, A. N., Johnson, C. G., Gjaltema, C., Clavel, P., & Gray, J. M. N. T. (2017). Multiple solutions for granular flow over a smooth two-dimensional bump. *Journal of Fluid Mechanics*, *815*, 77–116. https://doi.org/10.1017/jfm.2017.41

Wetter, C., Walter, F., McArdell, B. W., Blumenschein, F., Spielmann, R., Aaron, J., et al. (2026). Formation, propagation, and annihilation of surge waves in debris flows. *Engineering Geology*, *367*, 108648. https://doi.org/10.1016/j.enggeo.2026.108648

Woodhouse, M. J., Thornton, A. R., Johnson, C. G., Kokelaar, B. P., & Gray, J. M. N. T. (2012). Segregation-induced fingering instabilities in granular free-surface flows. *Journal of Fluid Mechanics*, *709*, 543–580. https://doi.org/10.1017/jfm.2012.348

21699011, 2026, 10, Downloaded from https://agupubs.onlinelibrary.wiley.com/doi/10.1029/2025JF008556 by The University Of Manchester, Wiley Online Library on [18/10/2026]. See the Terms and Conditions (https://onlinelibrary.wiley.com/terms-and-conditions) on Wiley Online Library for rules of use; OA articles are governed by the applicable Creative Commons License